

Photometric determination of the mass accretion rates of pre-main sequence stars.
VI. The case of LH 95 in the Large Magellanic Cloud*

KATIA BIAZZO,¹ GIACOMO BECCARI,² GUIDO DE MARCHI,³ AND NINO PANAGIA^{4,5}

¹*INAF - Osservatorio Astrofisico di Catania
Via Santa Sofia 78
I-95123 Catania, Italy*

²*European Southern Observatory
Karl-Schwarzschild-Str. 2
85748 Garching, Germany*

³*European Space Research and Technology Centre
Keplerlaan 1
2200 AG Noordwijk, Netherlands*

⁴*Space Telescope Science Institute
3700 San Martin Drive
Baltimore MD 21218, USA*

⁵*Supernova Limited
OYV #131, Northsound Rd.
Virgin Gorda VG1150, Virgin Islands, UK*

(Received September 13, 2018; Accepted March 12, 2019)

Submitted to ApJ

ABSTRACT

We report on the accretion properties of low-mass stars in the LH 95 association within the Large Magellanic Cloud (LMC). Using non-contemporaneous wide-band optical and narrow-band H α photometry obtained with the *Hubble Space Telescope*, we identify 245 low-mass pre-main sequence (PMS) candidates showing H α excess emission above the 4σ level. We derive their physical parameters, including effective temperatures, luminosities, masses (M_*), ages, accretion luminosities, and mass accretion rates (\dot{M}_{acc}). We identify two different stellar populations: younger than ~ 8 Myr with median $\dot{M}_{\text{acc}} \sim 5.4 \times 10^{-8} M_{\odot} \text{yr}^{-1}$ (and $M_* \sim 0.15 - 1.8 M_{\odot}$) and older than ~ 8 Myr with median $\dot{M}_{\text{acc}} \sim 4.8 \times 10^{-9} M_{\odot} \text{yr}^{-1}$ (and $M_* \sim 0.6 - 1.2 M_{\odot}$). We find that the younger PMS candidates are assembled in groups around Be stars, while older PMS candidates are uniformly distributed within the region without evidence of clustering. We find that \dot{M}_{acc} in LH 95 decreases with time more slowly than what is observed in Galactic star-forming regions (SFRs). This agrees with the recent interpretation according to which higher metallicity limits the accretion process both in rate and duration due to higher radiation pressure. The $\dot{M}_{\text{acc}}-M_*$ relationship shows different behaviour at different ages, becoming progressively steeper at older ages, indicating that the effects of mass and age on \dot{M}_{acc} cannot be treated independently. With the aim to identify reliable correlations between mass, age, and \dot{M}_{acc} , we used for our PMS candidates a multivariate linear regression fit between these parameters. The comparison between our results with those obtained in other SFRs of our Galaxy and the Magellanic Clouds confirms the importance of the metallicity for the study of the \dot{M}_{acc} evolution in clusters with different environmental conditions.

Corresponding author: Katia Biazzo
katia.biazzo@inaf.it

* Based on observations made with the NASA/ESA Hubble Space Telescope, obtained from the Data Archive at the Space Telescope Science Institute, which is operated by the Association of Universities for Research in Astronomy, Inc., under NASA contract NAS 5-26555.

Keywords: Accretion, accretion disks – Stars: formation – Stars: pre-main sequence – Galaxies: Magellanic Clouds – open clusters and associations: individual: LH 95 – Techniques: photometric

1. INTRODUCTION

In the current star formation paradigm of the magnetospheric accretion scenario, a central low-mass star grows in mass over time through accretion of material from a circumstellar disk of dust and gas funneled by stellar magnetic field, assumed to be mostly dipolar (e.g., Camenzind 1990; Königl 1991). The accretion disk is then truncated by the stellar magnetosphere at a few stellar radii (see a recent review on accretion onto pre-main sequence - PMS - stars by Hartmann et al. 2016). Reliable measurements of the rate at which mass from circumstellar disk is transferred onto the central PMS star is therefore important for understanding the evolution of both the star and its disk, and for tracing possible planetary formation and subsequent evolution. In particular, the study of how the mass accretion rate changes with time as a star approaches the main sequence, how it depends on the mass of the forming star, and how it is affected by the metallicity and density of the parent cloud or by the proximity of early-type stars are of particular interest.

Ground-based studies of Galactic nearby star-forming regions show a decrease of the mass accretion rate (\dot{M}_{acc}) with time, from $\sim 9 \times 10^{-8} M_{\odot} \text{yr}^{-1}$ at ~ 1 Myr to $\sim 6 \times 10^{-10} M_{\odot} \text{yr}^{-1}$ at ~ 10 Myr with a power law $\dot{M}_{\text{acc}}^{-1.2}$ (e.g., Sicilia-Aguilar et al. 2010). This behaviour is in line with the expected evolution of viscous disks (Hartmann et al. 1998; Rosotti et al. 2017; Mulders et al. 2017), but the spread of the data may exceed 2 dex at any given age. Such a scatter can be explained in part by the wide mass range covered by the observations, since the mass accretion rate depends also on the mass M_{\star} of the forming star. While during the last twenty years several authors discussed about the steepness of the one-power $\dot{M}_{\text{acc}} - M_{\star}$ relation (see, e.g., Alcalá et al. 2014, and references therein), recently, observations suggested that two different exponents for this relation, at different mass regimes, can better describe the data than a single power-law (Fang et al. 2013; Manara et al. 2017; Alcalá et al. 2017), and this behaviour resembles theoretical predictions (Vorobyov & Basu 2009). In particular, for $M_{\star} > 0.2 M_{\odot}$ mass accretion rate was found to scale with the power of $\sim 1.3 - 1.4$ of the stellar mass. These latter works claim the importance of modelling self-gravity of the disks in the early evolution of the more massive systems, but also of other physical processes, such as photo-evaporation and planet formation

during young stellar objects lifetime may lead to disk dissipation on different timescales depending on stellar mass (see Alcalá et al. 2017, and references therein).

While potential systematic errors may contribute to the present uncertainty in the $\dot{M}_{\text{acc}} - M_{\star}$ relation, one of the main limitations of the ground-based observations comes from the relatively paucity of available measurements. Indeed, most of the results so far obtained are based on the mass accretion rates of some hundred stars, all located in nearby Galactic star forming regions (SFRs), covering a limited range of ages ($\sim 0.5 - 20$ Myr) and with essentially solar metallicity (see, e.g., Muzerolle et al. 1998; Herczeg & Hillenbrand 2008; Antonucci et al. 2011; Rigliaco et al. 2011; Biazzo et al. 2012; Costigan et al. 2012; Fang et al. 2013; Alcalá et al. 2014). The origin of this limitation can be found in the methods used to measure \dot{M}_{acc} . Indeed, current techniques based on medium-high resolution single-object spectroscopy or low-medium resolution multi-object spectroscopy (or UV photometry) of nearby regions limit the number of objects and the distance to the regions that can be observed (because, e.g., of crowding). To partially overcome these limitations, De Marchi et al. (2010) have developed and tested to the SN 1987A field a new method to reliably measure the mass accretion rate from photometry. This method, successfully applied to several regions of the Large Magellanic Cloud (Spezzi et al. 2012; De Marchi et al. 2017), the Small Magellanic Cloud (De Marchi et al. 2011, 2013), and the Milky Way (Beccari et al. 2010, 2015; Zeidler et al. 2016), combines wide-band V and I photometry with narrow-band $H\alpha$ imaging to identify all stars with significant $H\alpha$ excess emission and to derive from it the accretion luminosity (L_{acc}) and hence \dot{M}_{acc} for many hundreds of objects all at once.

Here, we apply the same method to the young association LH 95. This region, first identified by Lucke & Hodge (1970), is one of the stellar aggregates located north of the Large Magellanic Cloud (LMC) at $\alpha \sim 5^{\text{h}}37^{\text{m}}04^{\text{s}}.32$ and $\delta \sim -66^{\circ}22'00''.7$ in $J2000$. This group was recognized by Kontizas et al. (1994) as an association rather poor in total number of stars and low in density ($\sim 0.05 - 0.07 M_{\odot} \text{pc}^{-3}$). It is embedded in the bright H II region LH α 120/N 64C (Henize 1956), in an area situated to the north-east of the superbubble LMC 4. Lucke (1974) detected four early-type stars ($B - V \sim 0$) with $13 < V < 16$ mag, while Konti-

zas et al. (1994) counted in it 15 blue stars and estimated for the region a mean age of $2 \pm 1 \times 10^7$ yr.

Most recently, Gouliermis et al. (2002) determined a diameter slightly higher than about $2'$ for LH 95. From the $R - H\alpha$ color index versus the color index $B - V$, they identified a central cluster of four Be stars which strongly determine the H II emissivity in an area of $\sim 4'.1 \times 5'.3$. They estimated a reddening of $0.1 - 0.2$ mag in $B - V$ color and an age as young as ~ 8 Myr within the cluster and older than ~ 50 Myr in the field. They discuss about the possibility that LH 95 is not a large mass segregated system, but rather a small young system. Studies on the initial mass function from high-mass ($\sim 70 M_\odot$) down to sub-solar ($\sim 0.4 M_\odot$) regime were led by Da Rio et al. (2009, 2012), while claims about the possibility of age spread within the PMS stars in the associations were reported by Da Rio et al. (2010).

Thanks to the high angular resolution and wide field achievable with the instruments on board of the *Hubble Space Telescope* (HST), several LMC associations containing PMS candidates were identified (Gilmozzi et al. 1994; Romaniello 1998; Panagia et al. 2000; Romaniello et al. 2006; Gouliermis et al. 2006, 2007; De Marchi et al. 2010, 2017; Spezzi et al. 2012). The spatial distribution of PMS stars within LMC associations shows the existence of significant substructures, as in the case of Galactic OB associations. Moreover, the locations of the detected low-mass PMS stars on color-color diagrams are found to be in excellent agreement with those of T Tauri stars with $\lesssim 2 M_\odot$ in young associations of the Milky Way (Briceno et al. 2007). Gouliermis et al. (2007) analyzed the stellar content of LH 95 finding for the association a mass distribution from bright OB stars ($\sim 7 M_\odot$) to faint red PMS stars ($\sim 0.3 M_\odot$). They found that the PMS members of this association seem to be clustered in stellar sub-groups containing also a few early-type stars.

In the present paper, we study the LH 95 association taking advantage of the HST photometry in three bands. In Section 2, we describe the photometric observations, while in Section 3 we address the identification of PMS candidates via their color excess, the measurement of the $H\alpha$ luminosity, and the derivation of the stellar parameters. Section 4 shows how L_{acc} and \dot{M}_{acc} is obtained from the $H\alpha$ luminosity. A general discussion about our results is provided in Section 5, while summary and conclusions are drawn in Section 6. The Appendix A provides a discussion of how stellar mass, age, mass accretion rate change using different evolutionary tracks, while Appendix B lists the stellar and accretion parameters of the selected low-mass PMS candidates.

2. PHOTOMETRIC OBSERVATIONS

The data were collected as part of HST programs #10566 (PI: Gouliermis), #12872 (PI: Da Rio), and #13009 (PI: De Marchi). The LH 95 region was observed with the Wide-Field Channel (WFC) of the Advanced Camera for Surveys (ACS) in the narrow-band filter $F658N$ (centered on the $H\alpha$ line) and in the wide-band filters $F555W$ and $F814W$, equivalent to the standard Johnson V and I bands, respectively. A log of the ACS/WFC observations is given in Table 1. A color-composite image of the region in the filters $F555W$ and $F814W$ is shown in Fig. 1. These $F555W$ and $F814W$ band observations are among the deepest ever taken toward the LMC (see Gouliermis et al. 2007; Da Rio et al. 2009) and will allow us to explore photometrically the accretion properties for these resolved extragalactic low-mass PMS stars.

The entire data-set was reduced using the package DAOPHOTII (Stetson 1987). We used more than 30 well sampled and not saturated sources to model the point spread function (PSF) of all the $F555W$ and $F814W$ images. We then used the task DAOPHOTII/MONTAGE to stack all the $F555W$ and $F814W$ images together in order to produce a deep image cleaned from cosmic rays and detector imperfections. We used the stacked image to create a master list of sources. We accepted all objects identified at 5σ above the background. The master list was used to perform accurate PSF fitting photometry on each single frame using the task ALLFRAME (Stetson 1994). In order to retain a source in our final catalogue we require that the object is detected in at least 3 out of 5 images both in the $F555W$ and $F814W$ bands. The average of the magnitudes measured in each individual frame was adopted as stellar magnitude while the standard deviation was adopted as the associated photometric error.

Given the low level of stellar crowding affecting the images taken with the $F658N$ filter, we used aperture photometry to measure the m_{658} magnitude of the stars. Aperture photometry was obtained with DAOPHOTII using 5 deep drizzled images. These images are available for download as part of the high level scientific products of the archive of the Space Telescope Science Institute (STScI). We used the catalogue of sources measured in $F555W$ and $F814W$ as master list of stars. We registered the position of the stars listed in this catalogue on the astrometric system of the drizzled images with an overall accuracy of $0''.05$. Once again the average of the magnitudes measured in at least 3 out of 5 frames for every master list object was adopted as the stellar m_{658} magnitude in the final catalogue, while we took the

Table 1. Summary of the observations.

Program ID (#)	Date (yy-mm-dd)	UT (hh:mm:ss)	Filter	T_{exp} (s)
10566	2006-03-02	20:53:03	<i>F555W</i>	5200
10566	2006-03-06	20:59:47	<i>F814W</i>	5200
12872	2013-05-26	18:47:27	<i>F658N</i>	2718
12872	2013-05-28	03:07:15	<i>F658N</i>	2718
12872	2013-05-29	03:02:02	<i>F658N</i>	2862
12872	2013-05-30	01:20:39	<i>F658N</i>	2864
13009	2013-05-26	21:58:25	<i>F658N</i>	2753

resulting standard deviation around the mean for each object as the associated photometric uncertainty.

The final catalog contains 24515 objects with measured m_{555} and m_{814} magnitudes, of which 21512 have also a measure of m_{658} . This is expected as the images acquired with the *F658N* narrow filter are slightly shallower with respect to the broad-band images. We emphasize here that this is not an issue since we are here mostly interested in the identification of $H\alpha$ excess emitters, hence stars with high flux in the *F658N* band.

The m_{555} , m_{814} , and m_{658} magnitudes were calibrated in the VEGAMAG system following the recipe in Sirianni et al. (2005) and using the most recent zero point values available through the ACS Zeropoint Calculator (Ryon et al. 2018). As for the extinction law, we adopted the one derived specifically in the field of LH95 by Da Rio et al. (2009). The reddening distribution obtained by the same authors does not show evidence of patchy nature of the absorption, unlike other LMC (e.g., De Marchi et al. 2017) or nearby SFRs (see, e.g., Luhman 2007; Hillenbrand et al. 2013). Therefore, we applied a uniform reddening correction for all stars in the sample (details will be discussed in Sect. 3.1).

3. DATA ANALYSIS

In order to measure the $H\alpha$ luminosity, $L_{H\alpha}$, we need a solid estimate of the stellar continuum in the $H\alpha$ band, i.e. without the contribution of the emission from the background. This is important for deriving accretion luminosity and mass accretion rate, whose measurement will be discussed in the following sub-sections.

3.1. Identification of PMS candidates

With the aim to identify PMS candidates within LH95, we followed the method described and first tested in De Marchi et al. (2010) and then applied in a series of papers (Beccari et al. 2010, 2015; De Marchi et al. 2011, 2013, 2017; Spezzi et al. 2012; Zeidler et al. 2016). This

Table 2. Characteristics of the early-type stars identified in the field of our observations. Right ascension and declination are given in J2000.

Name	Right Ascension (hh:mm:ss)	Declination (°:':")	V/J (mag)
Sample of Be stars by Gouliermis et al. (2002)*			
ID114 ^a	05:37:05.38	-66:21:59.13	16.16 ^b
ID124 ^a	05:37:04.38	-66:22:00.53	16.24 ^b
ID157 ^a	05:36:59.33	-66:21:37.54	16.48 ^b
ID239 ^a	05:36:57.14	-66:21:48.53	16.87 ^b
ID410 ^a	05:37:03.57	-66:22:00.03	17.33 ^b
ID1388 ^a	05:37:02.08	-66:21:57.29	18.53 ^b
Sample of massive stars by Da Rio et al. (2012)**			
SK-66 170	05:36:58.945	-66:21:16.130	13.17 ^b
SK-66 172	05:37:05.553	-66:21:34.950	13.58 ^b
SK-66 174	05:37:15.723	-66:21:38.355	13.74 ^b
ID18 ^a	05:36:58.007	-66:21:42.613	14.53 ^b
ID85 ^a	05:37:15.129	-66:21:44.304	15.58 ^b
Sample of 2MASS stars by Cutri et al. (2003)			
2MASS J05370037-6623410	05:37:00.371	-66:23:41.03	13.254 ^c
2MASS J05365327-6623109	05:36:53.274	-66:23:10.98	14.846 ^c
2MASS J05370664-6622387	05:37:06.645	-66:22:38.73	14.212 ^c
2MASS J05370166-6622355	05:37:01.665	-66:22:35.55	14.653 ^c
2MASS J05370175-6623421	05:37:01.753	-66:23:42.15	14.554 ^c
2MASS J05370915-6621455	05:37:09.151	-66:21:45.59	14.813 ^c
2MASS J05370361-6621532	05:37:03.619	-66:21:53.22	14.848 ^c

* These objects were classified as Be stars by Gouliermis et al. (2002) through *BVR* photometry; ** These stars were classified as B0.2IIp, O2III(f*)+OB, O7.5III(f), O6.5V, and B1.5III, respectively, by Da Rio et al. (2012) using high-resolution spectroscopy.

^a Catalogue ID number of Gouliermis et al. (2002). ^b Magnitudes in *V* band. ^c Magnitudes in *J* band.

method relies on the detection of $H\alpha$ excess emission in low-mass star-forming stars (see, e.g., Königl 1991).

We selected from our photometric catalogue in the *F555W*, *F658N*, and *F814W* bands all those stars whose photometric uncertainties δ_{555} , δ_{658} , and δ_{814} in each individual band do not exceed 0.05 mag. A total of 1294 stars satisfy this condition (grey small dots in the color-color diagram of Fig. 2), out of 24515 sources in the complete catalogue (black little dots in the color-magnitude diagram of Fig. 3). These stars are typically old main sequence (MS) and do not have appreciable $H\alpha$ excess; they define the reference with respect to which one should look for excess emission in the $(m_{555} - m_{658})_0$ color at given $(m_{555} - m_{814})_0$ color (see the running median represented by the dashed line in Fig. 2). For comparison, this reference sequence is in good agreement with the theoretical color relationship in the same filters obtained using the Bessell et al. (1998) model atmospheres for MS stars with effective temperature $3500 \leq T_{\text{eff}} \leq 40000$ K, surface gravity $\log g = 4.5$, and metallicity index $[M/H] \simeq -0.5$ (Colucci et al. 2012), appropriate for the LMC (dotted line in the same figure). The root mean square (rms) deviation between the model and the data amounts to ~ 0.03 mag and is dominated by the systematic depar-

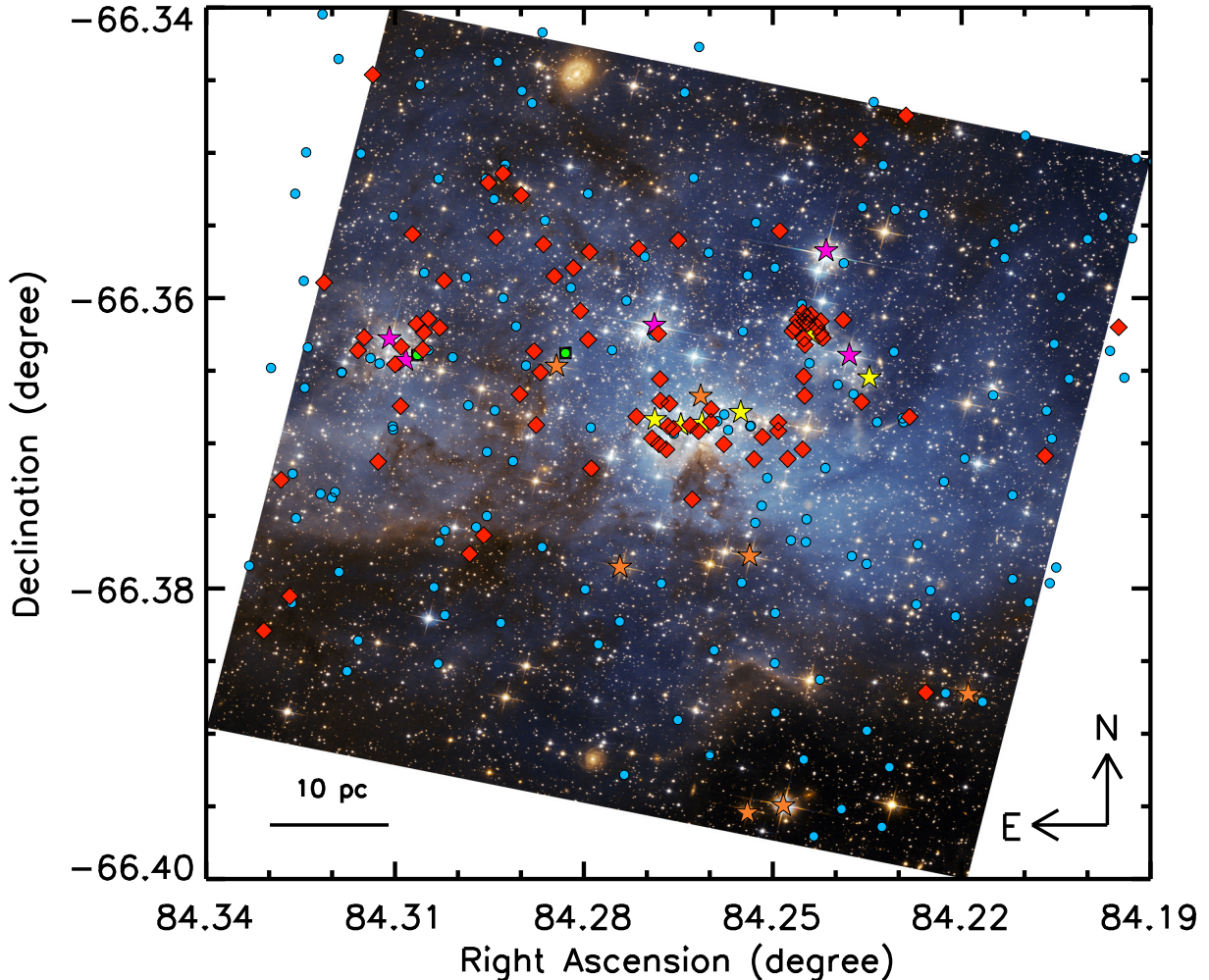


Figure 1. Color-composite image from ACS/WFC observations in the $F555W$ and $F814W$ filters of LH 95. Stars showing $H\alpha$ excess are displayed with filled dots and diamonds, the latter representing the younger pre-main sequence candidates; green squares are the two bright early-type targets excluded from our analysis (see Sect. 3.1 for the selection criteria of PMS candidates). Star symbols mark the position of B stars identified by Gouliermis et al. (2002) (yellow), OB stars analyzed by Da Rio et al. (2012) (purple), probable massive young targets selected from the 2MASS catalogue (Cutri et al. 2003) with $J - H < 0.8$ and $J < 15$ mag (orange). These early-type stars are listed in Table 2. North is up and East to the left. The field covers an area of about $0^\circ.15 \times 0^\circ.06$. [Picture credits: NASA, ESA, and the Hubble Heritage Team (STScI/AURA)-ESA/Hubble Collaboration; Acknowledgment: D. Gouliermis (Max Planck Institute for Astronomy, Heidelberg).]

ture around $(m_{555} - m_{814})_0 \sim 1.5$ most likely due to the coarse sampling of our data. As pointed out by De Marchi et al. (2017), even before correction for reddening, such a kind of color-color diagram provides a robust identification of stars with $H\alpha$ excess, since in these bands the reddening vector runs almost parallel to the median photospheric colors of non-accreting objects, and, moreover, our targets do not have a known patchy nature of the interstellar absorption (see Da Rio et al. 2009).

To select the most probable accretors, after the exclusion of the 1294 stars taken as reference, we first selected the targets with $\delta_{555} < 0.1$ mag, $\delta_{658} < 0.3$ mag, and

$\delta_{814} < 0.1$ mag, namely 5155 objects. Then, we retained those whose de-reddened $(m_{555} - m_{658})_0$ color exceeds the local average by at least four times the individual combined photometric uncertainty δ_3 in the color in the three bands $F555W$, $F658N$, and $F814W$, where

$$\delta_3 = \sqrt{\frac{\delta_{555}^2 + \delta_{658}^2 + \delta_{814}^2}{3}}, \quad (1)$$

with δ_{555} , δ_{658} , and δ_{814} being the photometric uncertainties in each individual band. It should be noted that, for the selected 5155 sources, δ_3 is dominated by the uncertainty on the $H\alpha$ magnitude, which is on average around 0.15 mag, while the median value of the uncer-

tainty in the other two bands is $\langle \delta_{555} \rangle \sim 0.03$ mag and $\langle \delta_{814} \rangle \sim 0.02$ mag, respectively. In the end, a total of 247 stars satisfy the condition that we have set and they must be regarded as having bona fide $H\alpha$ excess above the 4σ level (big dots in Fig. 2). This allows us to select most probable PMS candidates even when the uncertainty in the $F658N$ band is not negligible. Indeed, as we will show in Sect. 3.2, our selection in $H\alpha$ excess emission translates directly into $H\alpha$ equivalent widths typical of accretors, allowing us to safely remove possible contaminants from our sample, such as chromospherically active stars (see, e.g., White & Basri 2003; Biazzo et al. 2007; Frasca et al. 2008; Beccari et al. 2015). Other classes of objects whose spectra might present $H\alpha$ emission are interacting binaries, but typically they are very rare in Local Group galaxies (e.g., Dobbie et al. 2014) and their intrinsic colors are bluer with respect to the main sequence (see, e.g., Beccari et al. 2014, and references therein).

The m_{555} magnitude versus the $m_{555} - m_{814}$ color of the detected sources is shown in Fig. 3. From this color-magnitude diagram, the two targets with $m_{555} < 22$ mag are bright objects with $H\alpha$ excess, that we exclude from our following analysis as we are searching for low-mass PMS candidates¹. Gouliermis et al. (2007) found in the CMD a pronounced turnoff at $V \sim 22.5$ mag and a red clump at $V \sim 19$ mag and $V - I \sim 1.2$. The red clump (RC) and old MS population are best matched by a 0.7 Gyr isochrone taken from the Padova-Trieste Stellar Evolution Code (PARSEC; see Bressan et al. 2012). Stars with $H\alpha$ excess are shown in red and they define two distinct groups, nicely separated by a 8 Myr old PMS isochrone from the same authors. The theoretical isochrones of Bressan et al. (2012) are shown, respectively, with solid blue and orange dashed lines in Fig. 3, where the distance of 51.4 ± 1.2 kpc (Panagia 1999), corresponding to a distance modulus $(m_V - M_V)_0 = 18.55$, and a metallicity of $Z = 0.007$, typical of young LMC stars (e.g., Colucci et al. 2012) were adopted. These isochrones includes both the effects of the Milky Way intervening absorption along the line of sight and the LH 95 mean absorption within the field. According to Fitzpatrick & Savage (1984), the former amounts to $A_{555}^{\text{MW}} = 0.22$ mag and $E(m_{555} - m_{814})^{\text{MW}} = 0.1$, while for the LH 95 field we

¹ Even though we could derive the parameters of these two objects from their colors, we prefer to focus only on low-mass objects. In fact, without spectroscopy the age of these early-type stars would be rather uncertain, because they could be both PMS and post-MS stars, making the comparison with the lower-mass PMS objects of interest here more difficult.

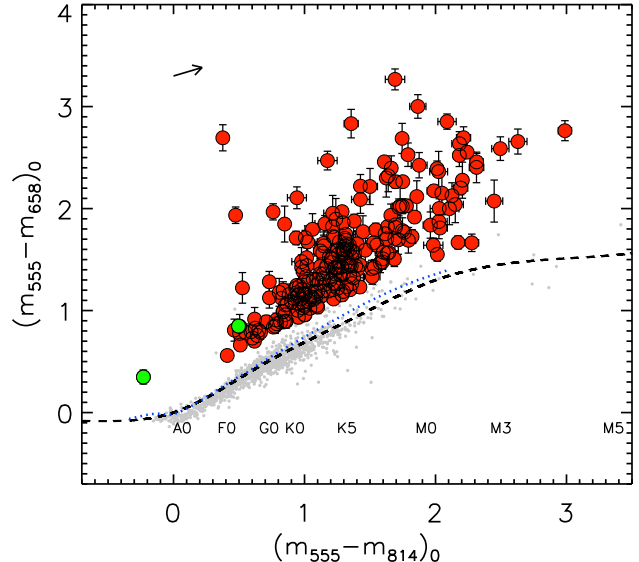


Figure 2. De-reddened color-color diagram of the selected 1541 stars in the field of LH 95. All magnitudes are already corrected for both the extinction contribution of our Galaxy and of LH 95. The dashed line represents the running median photospheric $(m_{555} - m_{814})_0$ color for the 1294 stars with small (< 0.05 mag) photometric uncertainties in all three bands (grey small dots). The dotted line shows the model atmospheres of Bessell et al. (1998) computed for the three ACS/WFC filters. The arrow displays the reddening vector of $E(m_{555} - m_{814})^{\text{LH95}} = 0.2$ and $E(m_{555} - m_{658})^{\text{LH95}} = 0.09$ for the adopted LH 95 extinction law. A total of 247 objects with $(m_{555} - m_{658})_0$ excess larger than 4σ are indicated with large red dots. Green dots mark the position of the two brightest ($\lesssim 22$ mag in the $F555W$ band) targets with $H\alpha$ excess emission. Error bars are also shown. Spectral types as in Pecaut & Mamajek (2013) are marked in the bottom of the plot.

considered the following mean extinction values (Da Rio et al. 2009): $R_{555} = A_{555}/E(m_{555} - m_{814}) \simeq 2.18$ and $R_{814} = A_{814}/E(m_{555} - m_{814}) \simeq 1.18$.

To determine the presence and extent of possible differential extinction, Da Rio et al. (2009, 2012) analyzed the position of the upper main sequence (UMS) stars in the CMD. In particular, after subtracting field stars, they compared the CMD position of the UMS objects with that expected according to grids of evolutionary models. They concluded that there is not a significant level of differential extinction for the UMS stars in the LH 95 field. This conclusion is very relevant to our investigation because young PMS objects and UMS stars share the same spatial distribution (see, e.g., De Marchi et al. 2011, 2013). Those authors also provide the total optical extinction and reddening toward LH 95, namely, $A_{555}^{\text{tot}} = 0.6$ mag and $E(m_{555} - m_{814})^{\text{tot}} \sim 0.3$,

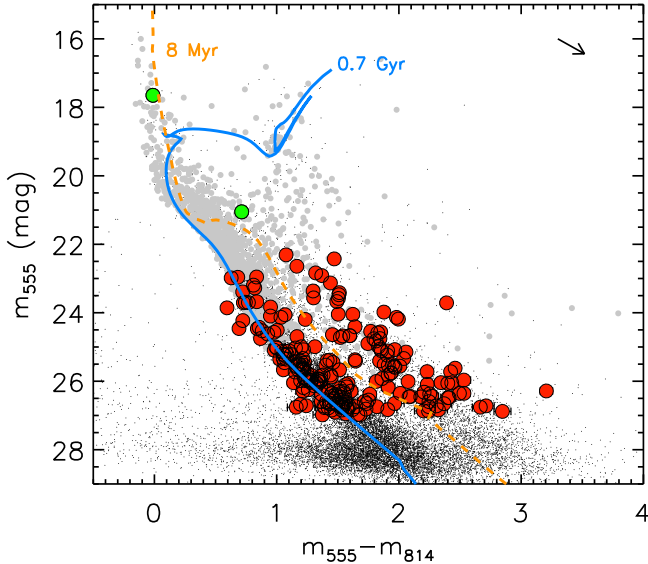


Figure 3. Color-magnitude diagram of the field of LH 95 (24515 sources). All magnitudes are already corrected for the extinction law of our Galaxy. As in Fig. 2, green and red big dots represent the 247 PMS star candidates with $H\alpha$ excess emission at the 4σ level with m_{555} magnitude brighter and fainter than 22 mag, respectively, while small grey dots are, as in Fig. 2, the stars with photometric uncertainties < 0.05 mag in all three filters (see text). Error bars are also shown, but they are within the symbol size in most cases. The arrow is the reddening vector of $E(m_{555} - m_{814})^{\text{LH95}} = 0.2$ and $A_{555}^{\text{LH95}} = 0.44$ mag applicable to LH 95. Solid and dashed lines show the theoretical isochrones from Bressan et al. (2012) for ages of 0.7 Gyr and 8 Myr, respectively, metallicity $Z = 0.007$, and a distance modulus $(m_V - M_V)_0 = 18.55$. These models include only the absorption due to our Galaxy along the line of sight (i.e. $E(m_{555} - m_{814})^{\text{MW}} = 0.1$ and $A_{555}^{\text{MW}} = 0.22$ mag).

respectively; therefore the reddening within LH 95 is $E(m_{555} - m_{814})^{\text{LH95}} \sim 0.2$. Finally, considering the relation $A_{658}/A_{555} \simeq 0.8$ (Rodrigo et al. 2012) and the adopted Galactic and LMC extinction laws, the total extinction in the $H\alpha$ band toward LH 95 is $A_{658} = 0.48$ mag.

Looking at the color-magnitude diagram shown in Fig. 3, most stars with $m_{555} - m_{814} \gtrsim 0.6$ and $m_{555} \gtrsim 22$ mag could be old MS, or PMS objects, or red giants. This is why it is important to search for PMS objects analyzing the $H\alpha$ excess emission as signature of accretion (and therefore of youth).

3.2. From $H\alpha$ color excess to line luminosity and equivalent width

As pointed out by De Marchi et al. (2010), the contribution of the $H\alpha$ line to the m_{555} magnitude is com-

pletely negligible and therefore the magnitude $\Delta H\alpha$ corresponding to the excess emission is:

$$\Delta H\alpha = (m_{555} - m_{658})^{\text{obs}} - (m_{555} - m_{658})^{\text{ref}}, \quad (2)$$

where the superscript “obs” refers to the observations and “ref” to the reference sequence at each $m_{555} - m_{814}$ color (dashed line in Fig. 2). Once $\Delta H\alpha$ is derived in this way, the $H\alpha$ emission line luminosity $L_{H\alpha}$ can be immediately obtained from the photometric zero point (ZP), the absolute sensitivity of the instrumental setup (in this case the $F658N$ of the ACS/WFC), and the distance to the sources. We took the $F658N$ photometric properties of the instrument at the exact observing dates from Ryon et al. (2018), namely the inverse sensitivity $PHOTFLAM = 1.967 \times 10^{-18}$ erg cm $^{-2}$ s $^{-1}$ Å, and the zero-point in VEGAMag $ZP = 22.383$ mag. Considering the rectangular width of the $F658N$ filter $RECTW = 74.98$ Å and assuming a distance to SN 1987A of 51.4 ± 1.2 kpc (Panagia 1999), we derived a median value of the $H\alpha$ luminosity of the 245 low-mass objects with $H\alpha$ excess of $\sim 1.2 \times 10^{31}$ erg s $^{-1}$ or $\sim 0.3 \times 10^{-2} L_{\odot}$. This value is lower than that measured by De Marchi et al. (2010) in the SN 1987A field ($\sim 10^{-2} L_{\odot}$) and that found by De Marchi et al. (2017) in the 30 Doradus Nebula ($\sim 3 \times 10^{-2} L_{\odot}$). This difference is not surprising because our observations include stars with greater $m_{555} - m_{814}$ colors, and therefore lower masses.

The total uncertainty on our $L_{H\alpha}$ measurements is typically $\sim 16\%$ and is dominated by the inaccuracy on the $H\alpha$ magnitude, the uncertainty on the distance and on the instrumental setup accounting for $\sim 5\%$ and $\sim 3\%$, respectively (see also De Marchi et al. 2010). Extinction indeed does not have any influence in the $V - H_{H\alpha}$ color excess, and therefore in the $L_{H\alpha}$ uncertainty, both because the reddening vector in Fig. 2 is substantially parallel to the reference template (dashed line) and also because our targets do not seem to have differential reddening, as indicated, for instance, by the relatively compact RC in the CMD.

Following De Marchi et al. (2010), the difference between the observed $H\alpha$ magnitude (m_{658}) and the level of the $H\alpha$ continuum (m_{658}^c) provides a direct measure of $EW_{H\alpha}$. In particular, since the line width is narrow compared to the width of the filter, the line profile falls completely within the filter bandpass. If we assume that the stars defining the reference template have no $H\alpha$ absorption features, their $m_{555} - m_{658}$ index would corre-

spond to the color of the pure continuum. Therefore, $EW_{H\alpha}$ is given by the following relationship:

$$\begin{aligned} EW_{H\alpha} &= RECTW \times [1 - 10^{-0.4 \times (m_{658} - m_{658}^c)}] \\ &= RECTW \times [1 - 10^{-0.4 \times \Delta H\alpha}], \end{aligned} \quad (3)$$

with $RECTW$ the rectangular width of the $F658N$ filter. As for $L_{H\alpha}$, the statistical uncertainty on $EW_{H\alpha}$, typically $\sim 6\%$, is dominated by the uncertainty on the $H\alpha$ photometry. The validity of this method was also independently tested and then confirmed by [Barentsen et al. \(2011, 2013\)](#), who considered both photometric and spectroscopic observations for T Tauri stars in the Galactic NGC 2264 and IC 1396 young regions. The authors found strong correlation between $H\alpha$ equivalent widths derived with both spectroscopic and photometric methods. This already suggests that the possible contribution of veiling due to accretion is greatly reduced by the subtraction of the continuum flux from the band flux.

During the last thirty years, veiling was more and more accurately measured mainly thanks to spectroscopic observations of SFRs in our Galaxy (see, e.g., [Hartigan et al. 1995](#); [Manara et al. 2013](#); [Alcalá et al. 2014](#), to cite a few works), but in general, its effects must be taken into account also for broad-band measurements. As discussed in detail in [De Marchi et al. \(2010\)](#), any nebular continuum unrelated to the stellar photosphere (and therefore also the one associated with the accretion luminosity) will add to the intrinsic continuum of the stars, thereby affecting both the observed total level and the slope. This could alter the measured broadband colors of the source, thereby thwarting our attempts to infer the level of the continuum in the $H\alpha$ band from the observed m_{658} and m_{814} magnitudes, and ultimately also affecting the effective temperature and bolometric luminosities that we measure (see Section 3.3.1).

Fortunately, the contribution of the nebular continuum appears to be insignificant for the stars in our sample. To prove this, [De Marchi et al. \(2010\)](#) assumed a fully ionized gas of pure H, considering only bound-free and free-free transitions and ignoring the contribution to the continuum from two-photon emission ([Spitzer & Greenstein 1951](#)). Using [Osterbrock's \(1989, chapter 4\)](#) tabulations, they find $H\alpha$ line intensity and $H\alpha$ continuum fluxes of the nebular gas for gas electron temperatures in the range 5000–20000 K (see their Table 2). The purely nebular $EW_{H\alpha}$ ranges from 5000 Å to 9000 Å, or more than 2 orders of magnitude higher than what we measure for our PMS objects (see Figure 4). We can,

therefore, safely conclude that the nebular contribution to the continuum is negligible (less than 1%).

Furthermore, for gas temperatures in the range 5000–10000 K the $m_{658} - m_{814}$ color of the nebular continuum varies from 1.4 to 0.5, spanning a range typical of GK type stars. Thus, the effects of the nebular continuum on the $m_{658} - m_{814}$ color of PMS stars remains insignificant even for the objects with the highest $EW_{H\alpha}$ in our sample. Therefore, for these objects also the relationships between $m_{658} - m_{814}$ and effective temperature and, in turn, the bolometric luminosity that we will derive in Section 3.3.1 are not affected by the veiling introduced by the additional nebular continuum.

The values of $EW_{H\alpha}$ that we obtain in the field of LH 95 are shown in Fig. 4 as a function of the dereddened $m_{555} - m_{814}$ color for the 245 low-mass PMS candidates. All selected targets at the 4σ level fall well above the threshold established by [White & Basri \(2003\)](#) to identify probable accretors as a function of spectral type (see also [Beccari et al. 2014](#)), thus confirming that our selection criteria of PMS candidates is cautious. Indeed, the sample that we selected must be considered as a lower limit to the number of objects with genuine $H\alpha$ excess. This means that most probably we are excluding from the sample the weakly accreting PMS stars, but completeness is not the aim of this work. Instead, we are interested in studying the properties of the mass accretion process in PMS stars and for this reason it is important to have a solid sample of candidates.

Values of $EW_{H\alpha}$ for our sample range from ~ 12 Å to ~ 70 Å, with a median of 29 Å. These values are typical of PMS stars. It should be noted that, because of the width of the specific $F658N$ filter, $\Delta H\alpha$ includes small contributions due to the emission of the two forbidden [N II] lines at $\lambda 6548$ Å and $\lambda 6584$ Å. [De Marchi et al. \(2010\)](#), following a conservative approach, have estimated corrections of ~ 0.98 , on average, for the ACS $F658N$ filter. This translates into a lower $EW_{H\alpha}$ value by $\sim 0.2 - 1.4$ Å in the range characteristic of our targets, i.e. within the uncertainties of our measurements (see Table 3).

3.3. Astrophysical parameters of PMS candidates

Physical parameters of the PMS candidates identified in Section 3.1, i.e. their effective temperature, bolometric luminosity, mass, and age, were obtained as explained in the following two sub-sections.

3.3.1. Effective temperature and bolometric luminosity

We derived the effective temperature T_{eff} from the observed $m_{555} - m_{814}$ color, properly corrected for the total reddening, due to both our Galaxy and LH 95, as explained in Section 3.1. The models of [Bessell et al.](#)

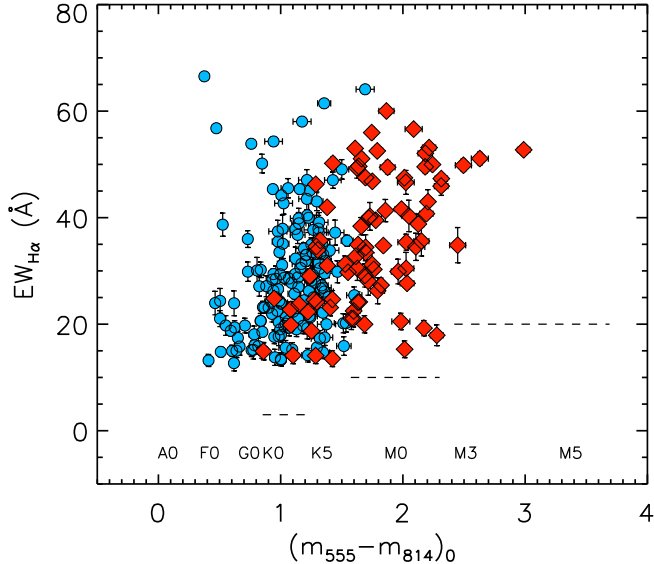


Figure 4. $H\alpha$ equivalent width of the selected 245 low-mass PMS candidates in the field of LH 95, as a function of the dereddened $m_{555} - m_{814}$ color. The red diamonds mark the position of the younger PMS candidates while the blue dots represent the older PMS stars in our sample with $H\alpha$ excess (see Section 3.3 for details). Error bars are also shown. Spectral types as in Pecaut & Mamajek (2013) are marked at the bottom of the plot. Dashed lines define the thresholds above which most probable accretors are positioned at given spectral types, according to White & Basri (2003).

(1998) with $3500 \text{ K} \leq T_{\text{eff}} \leq 40000 \text{ K}$, $\log g = 4.5$, and metallicity index of $[M/H] = -0.5$ dex were used for the conversion from color to effective temperature, following the work by De Marchi et al. (2010) for ACS/WFC filters (see that paper for details). Since models of Bessell et al. (1998) are available only for $T_{\text{eff}} > 3500 \text{ K}$, for lower temperatures we decided to consider the $T_{\text{eff}} - (V - I_C)$ calibration by Pecaut & Mamajek (2013)², assuming for simplicity that the calibrated m_{555} and m_{814} magnitudes coincide with V and I_C . The reason for using a different calibration at temperatures lower than those covered by the models of Bessell et al. (1998) is to avoid possibly larger uncertainties in T_{eff} due to arbitrary extrapolations, as the relationship between T_{eff} and $m_{555} - m_{814}$ is critical for very cool temperatures. The bolometric luminosity L_\star was obtained from the m_{555} magnitude corrected for the interstellar extinction (see Section 3.1), having adopted a distance to LH 95 of

² We verified that in the T_{eff} range in common, the two calibrations are in very good agreement. In particular, considering the parameter space of the present work, the agreement is within ~ 0.03 mag and $\sim 70 \text{ K}$ in color and T_{eff} , respectively.

51.4 kpc (Panagia 1999) and a bolometric solar magnitude $M_{\text{bol}}^\odot = 4.74$ mag (Pecaut & Mamajek 2013), and having applied at any T_{eff} the bolometric corrections of the latter authors.

The positions of the PMS candidates in the HR diagram are displayed in Fig. 5, where the $\pm 1\sigma$ uncertainties on T_{eff} and L_\star are also shown; in most cases, these errors are within the symbol size. They are mostly due to uncertainties in photometry and distance³. As reference, we traced the PMS theoretical isochrones of Bressan et al. (2012) for metallicity $Z = 0.007$, as appropriate for the young populations of the LMC (e.g., Colucci et al. 2012), and for ages of 1, 8, 16, 32 Myr from right to left (dot-dashed lines). Also shown are the representative PARSEC evolutionary tracks for masses of 0.1, 0.2, 0.4, 0.6, 0.8, 1.0, 1.2, 1.5, 2.0, 3.0, and 4.0 M_\odot from the same Bressan et al. (2012) models (solid lines). The dashed line in the same figure defines the Zero Age Main Sequence (ZAMS) by Bressan et al. (2012). From the stellar bolometric luminosity and effective temperature we also derived the stellar radius R_\star assuming 5770 K as effective temperature of the Sun. Typical mean uncertainties on R_\star are around 5% and include both uncertainties in T_{eff} and L_\star .

In the HR diagram of our PMS candidates, a bimodal distribution in age and T_{eff} seems to be evident, with a separation around 8 Myr. In particular, stars younger than 8 Myr have a mean $T_{\text{eff}} \sim 3965 \text{ K}$, while older targets have a mean T_{eff} of $\sim 4990 \text{ K}$. This apparent bimodality will be also evident in the accretion properties, thus proving that it is not caused by detection limits. This issue will be discussed in the following Sections.

3.3.2. Mass and age

After having identified a population of PMS candidates in Sect. 3.1 and derived their effective temperature and bolometric luminosity in the previous sub-section, it is important for our purposes to determine their mass and age from the HR diagram (see Fig. 5). We followed the approach originally discussed in Romaniello (1998) and most recently refined by De Marchi et al. (2011, 2013). The method, without making assumptions on the properties of the population and on the pure basis of the measurement errors, provides the probability distribution for each individual star to have a given value of mass and age, with typical uncertainties of $\sim 5\%$ and $\sim 15\%$, respectively (see De Marchi et al. 2017 for a

³ Note that uncertainties on T_{eff} and L_\star do not include, respectively, possible color/magnitude temporal variability due to the observations in the $F555W$ and $F814W$ filters, having been obtained 4 days apart (see Table 1).

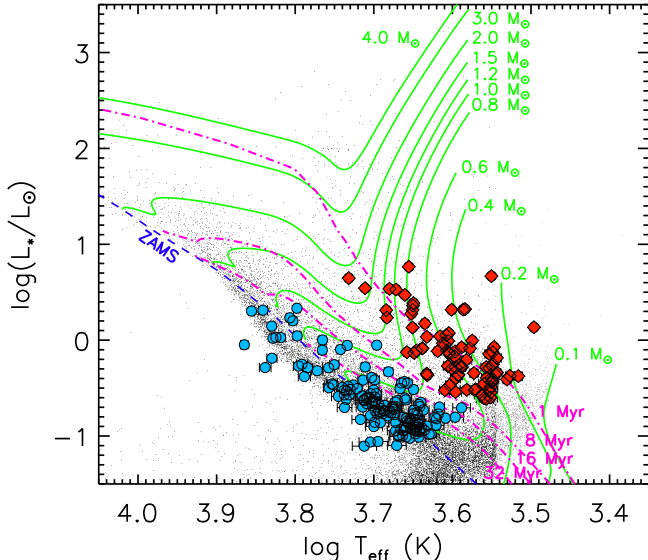


Figure 5. Location of the PMS candidates in the HR diagram (diamonds: younger PMS stars; dots: older PMS stars). Overimposed are the PARSEC evolutionary tracks (solid green lines) and theoretical isochrones (dot-dashed red lines) of Bressan et al. (2012) for metallicity $Z = 0.007$. The masses, in M_{\odot} , and the ages, in Myr, are indicated next to each track and isochrone, respectively. The position of the ZAMS is marked with a dashed line.

thorough explanation of the procedure). In particular, we determined the most likely mass M_{\star} of the 245 low-mass PMS candidates of LH 95 by comparing the location of each object on the HR diagram with theoretical PMS evolutionary tracks. As for the latter, we adopted the already mentioned PARSEC tracks for $Z = 0.007$ and available down to $M_{\odot} = 0.09M_{\odot}$ (Bressan et al. 2012).

Comparing masses computed from different evolutionary tracks is important for the determination of the uncertainty on the mass accretion rate and of its relationship with stellar mass and age. In order to assess how differences in the evolutionary models affect our results, in Appendix A we compare mass, age, and mass accretion rate measurements obtained using the Pisa tracks from Tognelli et al. (2011), available down to $M_{\star} = 0.2M_{\odot}$, with those obtained using the PARSEC tracks. For an extensive discussion of the model-dependent age estimation in clusters, see the recent review by Soderblom et al. (2014).

We determined the ages of individual objects by interpolating between the isochrones in the HR diagram. As already mentioned in Section 3.1, from Fig. 5 it is evident that the PMS candidates appear to be distinct in two populations with a “gap” around 8 Myr. We thus

decided to divide the sample of selected PMS candidates in two sub-samples depending on their age: from now on we will indicate as *younger PMS candidates* those with age $t < 8$ Myr and *older PMS candidates* those with $t > 8$ Myr. With such an age difference, older PMS stars must belong to a previous generation with respect to the younger PMS objects, thus no spatial relationship (whether a correlation or anti-correlation) should be expected between the two types of objects, as indeed is evident in Fig. 1. This will be discussed in more details in Sect. 5.1. The younger PMS candidates are about 35% (85/245) of the total sample, while the older PMS candidates represent about 65% (160/245).

The histograms with the mass and age distributions for the 245 low-mass PMS candidates are shown in Fig. 6. Different line types correspond to younger (dashed lines) and older (dotted lines) PMS candidates. The mass distributions are peaked at similar values both for younger and older populations, but they show different ranges, with the younger population having wider range in mass than the older one. Not surprisingly, old PMS stars comprise many low-mass stars, since the more massive objects have already reached the MS. Inspecting the age distribution, a clear separation between younger and older PMS stars is evident. We highlight here that these measurements are not reliable to put constraints on the shape of the mass function or on the exact value of the star formation rate, since we are only considering PMS with $H\alpha$ excess emission at the 4σ level at the time of the observations. Moreover, we are not taking into account photometric incompleteness, which is unavoidably more severe at lower masses.

As already found by De Marchi et al. (2010, 2017) in other regions of the LMC, it is noteworthy that many of the PMS candidates in Fig. 5 are close to the MS and would have been missed if no information on their $H\alpha$ excess had been available. Since we would expect to find very young objects above and to the right of the MS in the CMD, it is indeed customary to identify PMS objects by searching in that area of the CMD. However, this method of identification of PMS stars is not very reliable, because of the presence of older populations and possible age spreads in the same field, which prevent the true identification of PMS stars on the basis of the stellar effective temperatures and luminosities alone (see discussion in De Marchi et al. 2010). In fact, these older PMS stars were not detected by Gouliermis et al. (2007) and were considered as field stars by the same authors.

In summary, we find evidence for a series of at least two star formation episodes, which correspond to two distinct stellar populations with different ages. We indeed identify a generation of younger PMS stars with

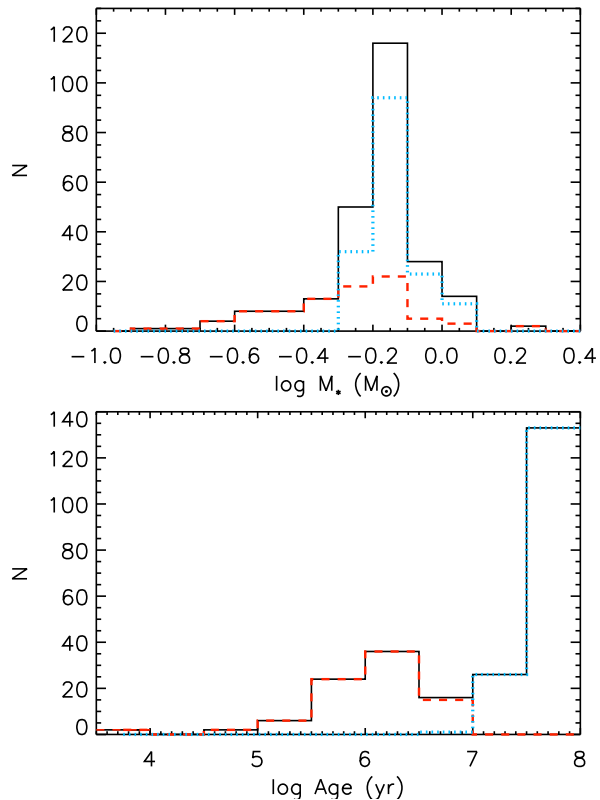


Figure 6. Histograms of the stellar mass (*upper panel*) and age (*lower panel*) for the 245 low-mass PMS candidates (solid lines). Dashed (red) and dotted (blue) lines correspond to the distributions of the younger and older populations, respectively.

ages ranging from < 1 Myr up to ~ 7 Myr (median value ~ 1 Myr) and a generation of older PMS stars with ages of $\sim 10 - 60$ Myr (median value ~ 50 Myr). Objects of this type are to be expected, also according to the evolutionary tracks. In fact, from the PARSEC tracks at metallicity $Z = 0.007$, a star with mass of $\sim 0.7 M_{\odot}$, i.e. around the peak histogram of our sample (see Fig. 6), takes ~ 50 Myr to reach the main sequence.

4. ACCRETION PROPERTIES

4.1. Accretion luminosity

In the magnetospheric accretion scenario, the accretion luminosity can be determined from the measurement of the reradiated energy from the circumstellar gas ionized and heated by the funnel flows (e.g., Hartmann et al. 1998). The $H\alpha$ line, and hence its luminosity, generated in this process can be used as a diagnostics to derive the accretion luminosity. From the analysis of a set of $L_{H\alpha}$ measurements of a group of T Tauri stars in Taurus-Auriga compiled by Dahm (2008), De Marchi et

al. (2010, 2013) found the following $L_{\text{acc}} - L_{H\alpha}$ relationship, that we adopt in this work:

$$\log L_{\text{acc}}/L_{\odot} = \log L_{H\alpha}/L_{\odot} + (1.72 \pm 0.25), \quad (4)$$

where the ratio $L_{\text{acc}}/L_{H\alpha}$ is linear. Recently, Alcalá et al. (2017), using X-shooter spectra of class II objects in the Galactic Lupus SFR, concluded that their relationships derived empirically between L_{acc} and the luminosity of several lines from UV to NIR are compatible with linear relationships.

Taking into account the Eq. 4, the median value of the accretion luminosity thus obtained for our sample of 245 low-mass PMS candidates is $\sim 0.17 L_{\odot}$. The statistical uncertainty on L_{acc} is dominated by the quoted uncertainty of $\sim 16\%$ on $L_{H\alpha}$ mainly associated with the photometric error in the $H\alpha$ magnitude. There is also a systematic error due to the $L_{\text{acc}} - L_{H\alpha}$ relationship, but since we used the Eq. 4 for all PMS stars, this uncertainty will not prevent the comparison between different targets. Comparable uncertainties in the $L_{\text{acc}} - L_{H\alpha}$ relationship were obtained by Alcalá et al. (2017) for the Lupus SFR.

4.2. Mass accretion rate

Once L_{acc} is known, the mass accretion rate \dot{M}_{acc} can be derived from the free-fall equation that links the luminosity released in the impact of the accretion flow with the rate of mass accretion according to the following relationship (see, e.g., Hartmann 1998):

$$\dot{M}_{\text{acc}} = \left(1 - \frac{R_{\star}}{R_{\text{in}}}\right)^{-1} \frac{L_{\text{acc}} R_{\star}}{GM_{\star}} \approx 1.25 \frac{L_{\text{acc}} R_{\star}}{GM_{\star}}, \quad (5)$$

where M_{\star} and R_{\star} are the stellar mass and the photospheric radius, respectively, R_{in} is the inner radius of the accretion disk, and G is the universal gravitational constant. R_{in} corresponds to the distance at which the disk is truncated, because of the stellar magnetosphere, and from which the disk gas is accreted and channeled by the magnetic field lines; therefore, its value is rather uncertain because it depends on how the accretion disk is coupled with the star. Following Gullbring et al. (1998), we assume $R_{\text{in}} = 5 R_{\star}$ for all PMS stars.

The median value of the distribution of mass accretion rates is $\sim 7.5 \times 10^{-9} M_{\odot} \text{ yr}^{-1}$, with higher values for the younger PMS candidates ($\sim 5.4 \times 10^{-8} M_{\odot} \text{ yr}^{-1}$) and lower values for the older PMS candidates ($\sim 4.8 \times 10^{-9} M_{\odot} \text{ yr}^{-1}$).

Concerning the statistical errors on \dot{M}_{acc} , the first source of uncertainty is $L_{H\alpha}$. With our selection criteria, the typical uncertainty on $L_{H\alpha}$ is $\sim 16\%$ and is

dominated by random errors. The other sources of uncertainty for \dot{M}_{acc} are the stellar mass and radius. The uncertainty on R_* is typically $\sim 5\%$, including the systematic uncertainty on the distance modulus. As for the mass, its determination is linked to the comparison of the location in the HR diagram with the evolutionary tracks. When we interpolate through the PMS evolutionary tracks to estimate the mass, the uncertainties on effective temperature and stellar luminosity imply an error of $\sim 7\%$ on M_* . Combining all the sources of errors, statistical uncertainty on \dot{M}_{acc} is $\sim 18\%$ ⁴.

The systematic uncertainty on \dot{M}_{acc} is dominated by the knowledge of the ratio $L_{\text{acc}}/L_{\text{H}\alpha}$ reported in the Equation 4. As already mentioned in Sect. 4.1, this ratio, even if uncertain by a factor of ~ 2 due to the variations of the H α line intensity, is the same for all stars, therefore the comparison between different objects is not hampered by this uncertainty, as long as the statistical errors are small (see De Marchi et al. 2010).

As pointed out by De Marchi et al. (2010), other sources of systematics errors on the derived \dot{M}_{acc} are due to theoretical evolutionary tracks and isochrones, reddening, H α emission generated by processes different from accretion, and contribution of nebular continuum to the photometric colors. Concerning the first source of errors, the main uncertainty on the derived mass and age comes from differences between models computed by different authors or from the use of models with metallicity that might not properly describe the stellar population under study. As shown in Appendix A, if we for instance had used the Tognelli et al. (2011) PMS tracks instead of those of Bressan et al. (2012) at the same metallicity, we would have obtained similar values of mass and age for PMS, to within 2% and 6% percent, with the largest discrepancy for $0.35 \lesssim M_* \lesssim 0.70 M_{\odot}$ (see Appendix A). Concerning the metallicity, had we used tracks with Z lower by 30%, the masses of our PMS objects would be systematically smaller by about 10% and the ages younger by a negligible amount for the luminosity and temperature ranges typical of our targets. For what concerns the reddening, we followed De Marchi et al. (2010), and concluded that underestimating the $E(m_{555} - m_{814})$

⁴ Our observations in $F555W$ and $F814W$ are not simultaneous to those in $F658N$ (see Table 1), thus implying that part of the scatter in \dot{M}_{acc} could be also due to intrinsic stellar variability. At timescales of a few years, as in our case, variations may be up to ~ 0.3 dex in $\log \dot{M}_{\text{acc}}$ (see Costigan et al. 2014). This is fully consistent with the observed 0.25 dex dispersion around the average relation between mass accretion rate and age for stars of similar mass reported by De Marchi et al. (2011). Intrinsic stellar variability of PMS candidates in several clusters of the Magellanic Clouds (including LH 95) will be the subject of a forthcoming work (De Marchi et al., in prep.).

color excess by ~ 0.2 mag would lead to a 30% overestimate of R_*/M_* . This translates into the same overestimate of \dot{M}_{acc} , which is smaller than the typical measurement uncertainties in the determination of the mass accretion rate. Finally, the possibility that processes different from accretion (e.g., chromospheric activity, H knots along the line of sight, ionization of H gas from nearby massive stars) or nebular continuum may alter the determination of \dot{M}_{acc} was addressed in detail in De Marchi et al. (2010), with the conclusion that their contribution is negligible. Indeed, the contribution of the background emission was safely removed thanks to the fact that the m_{658} magnitude of each star was determined above the background calculated locally in an annulus of few arcseconds around the centroid of the star (see also Section 2).

5. DISCUSSION

We will now explore the distribution of the accreting PMS candidates we identified in Sect. 3.1, how L_{acc} depends on stellar luminosity and effective temperature, and how \dot{M}_{acc} depends on stellar mass and age. Comparison between our results with those obtained in star-forming regions of our Galaxy and in the Large Magellanic Clouds will be also discussed.

5.1. Spatial distribution of accreting PMS stars

From a first inspection of the spatial distribution of the most probable accreting objects in LH 95 shown in Fig. 1, younger low-mass PMS candidates (red diamonds) appear to be clustered around Be stars. In particular, they are nonuniformly distributed in the field of the LH 95 association, but they are concentrated in small clusters around bright massive stars, with a clumpy spatial distribution on the scale of ~ 5 pc. Older PMS stars do not seem to form any significant concentration and are uniformly distributed within the region. Gouliermis et al. (2007) have suggested for LH 95 the existence of significant substructures of early-type stars containing candidate Herbig Ae/Be stars. Here, we support this scenario, but we also suggest that the sub-groups of early-type stars include also low-mass young PMS objects, similar to Galactic OB associations, like Orion (Briceño et al. 2005, 2019).

Besides very different ages, as discussed in Section 3.3.2, the two populations of younger and older PMS stars also have considerably different spatial density distributions. We compare these distributions in Fig. 7 by means of filled contours. In this figure, we considered the total population of 245 low-mass PMS candidates with well-defined masses and ages. The remarkable feature is the difference in the spatial distribution of younger and older PMS stars, with older objects

much more widely distributed and not overlapping with the younger generation.

The spatial distribution of the younger and strongly accreting PMS stars in Fig. 7 suggests that a recent star formation episode occurred a few Myr ago in regions including also many of the early-type Be stars identified in the LH95 field. The older and less accreting PMS stars are instead uniformly distributed without any specific clumping within the field. They might have formed several tens of Myr ago in a more central configuration but later have had time to dissipate in a widespread configuration. Their mean age of ~ 50 Myr and their spatial distribution within $\sim 40 - 50$ pc at the distance of LH95 (see also Fig. 1) is indeed compatible with a velocity dispersion of a few km s^{-1} , which is typical for young star-forming regions.

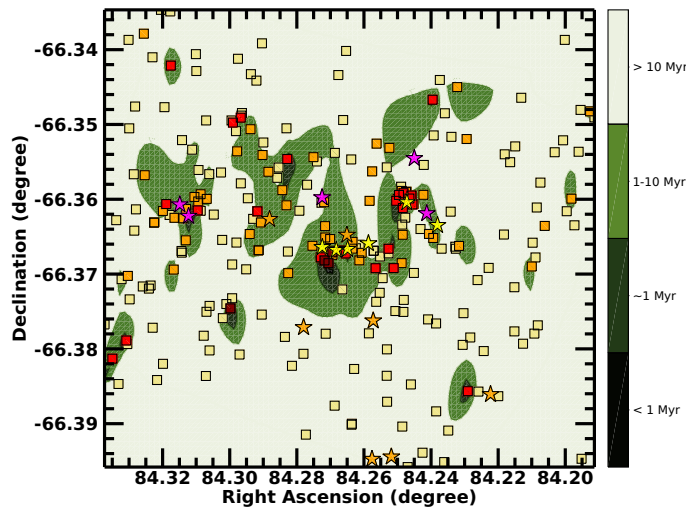


Figure 7. Spatial distribution of PMS candidates in the field of LH95. Squares are color coded by mass accretion rate, where more highly accreting PMS stars ($\dot{M}_{\text{acc}} \gtrsim 10^{-7} M_{\odot} \text{yr}^{-1}$) are marked with darker red. Filled contour regions colored in green show the position and density distribution of the PMS stars of different ages, with darker green regions corresponding to the density distribution of the youngest targets (< 10 Myr), as indicated in the bar on the right. The lighter green background corresponds to the distribution of the older PMS stars with ages of some tens of 10 Myr. As in Fig. 1, star symbols mark the position of Be stars identified by Gouliermis et al. (2002) (yellow), OB stars studied by Da Rio et al. (2012) (purple), probable massive young targets selected from the 2MASS catalogue (Cutri et al. 2003) with $J - H < 0.8$ and $J < 15$ mag (orange). North is up and East to the left.

5.2. Accretion luminosity versus stellar parameters

Figure 8 shows the accretion luminosity as a function of the stellar luminosity for both younger and older PMS stars. As already observed in SFRs close to the Sun, L_{acc} increases with the stellar luminosity, with a dispersion appearing to be even smaller for our targets (the recent case of the Lupus SFR by Alcalá et al. 2017 is shown as an example). The accretion luminosity of our PMS candidates mainly falls in the range between $0.2 L_{\star}$ and $\sim L_{\star}$, with a peak of the accretion luminosity distribution around $\sim 0.5 - 0.6 L_{\star}$, while those of regions in the solar neighbourhood, like the Lupus SFR by Alcalá et al. (2017) and overlaid in the figure, is typically $\lesssim 0.1 L_{\star}$ (see also, e.g., Muzerolle et al. 1998; White & Hillenbrand 2004; Antonucci et al. 2011; Caratti o Garatti et al. 2012; Biazzo et al. 2014). In this context, we cannot make a real quantitative comparison between our results and the findings by Alcalá et al. (2017), but it is possible that the differences between the samples could be mainly due to the following reasons: *i*) different selection criteria of accreting PMS candidates; *ii*) different methods to derive stellar parameters; *iii*) different $L_{\text{acc}}-L_{\text{H}\alpha}$ relationship, which can lead to differences up to $\sim 0.2 - 0.3$ dex in $\log L_{\text{acc}}/L_{\text{H}\alpha}$ (for instance, the $L_{\text{acc}}/L_{\text{H}\alpha}$ ratio in the case of the Alcalá et al. 2017 empirical relationship is not exactly linear as in our case); *iv*) different mass and metallicity ranges, our targets having $M_{\star} = 0.1 - 1.8 M_{\odot}$ (with a median of $\sim 0.7 M_{\odot}$) and $Z = 0.4 Z_{\odot}$, compared to $0.02 - 2.0 M_{\odot}$ (with a median of $\sim 0.2 M_{\odot}$) and $Z \sim Z_{\odot}$ for the Alcalá et al. (2017) sample; *v*) other environmental conditions, such as the gas density and contamination.

In Fig. 9, the L_{acc} values are plotted in logarithmic scale as a function of the effective temperature of our PMS candidates, together with the sample of Alcalá et al. (2017). The $L_{\text{acc}}-T_{\text{eff}}$ plot appears to be very similar to the HR diagram shown in Fig. 5, with the younger PMS and older PMS candidates well separated in T_{eff} . In the T_{eff} range between ~ 3.6 and ~ 3.7 some Lupus targets seem to have similar $\log L_{\text{acc}}/L_{\odot}$ values as our PMS stars. This could be an indication of similar accretion properties at given T_{eff} range, and therefore stellar mass. Unfortunately, we do not have many objects with very low effective temperatures (in particular with $\log T_{\text{eff}} < 3.5$) to verify the decreasing trend observed in Alcalá et al. (2017) at the very low-mass regime.

5.3. Mass accretion rate versus Age

In Fig. 10, the mass accretion rate is shown as a function of the stellar age. In this figure, we divided our sample in lower-mass and higher-mass targets, where $0.67 M_{\odot}$ is the median mass of all PMS candidates. At a first glance, the slope of the $\dot{M}_{\text{acc}}-\log t$ relationship ap-

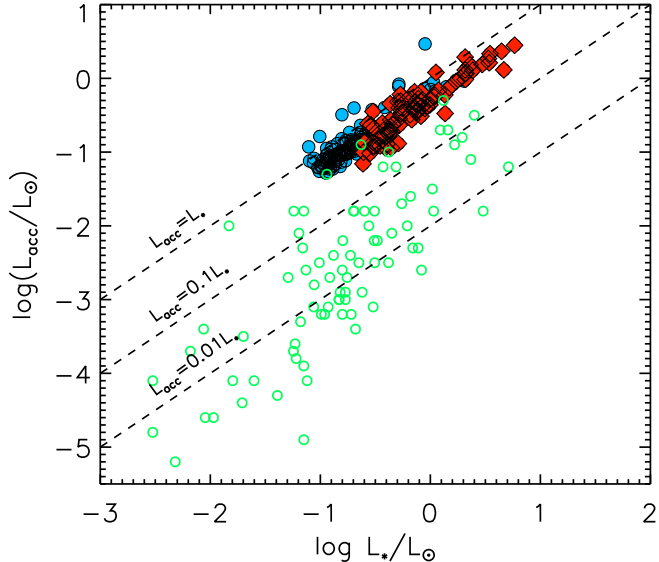


Figure 8. Accretion luminosity versus stellar luminosity. Circle and diamond symbols are as in Fig. 5. Dashed lines represent the loci of the three $L_{\text{acc}} - L_{\star}$ relations, as labeled. Open circles represent the Alcalá et al. (2017) sample of low-mass stars in the Galactic Lupus star-forming region observed with the X-shooter spectrograph.

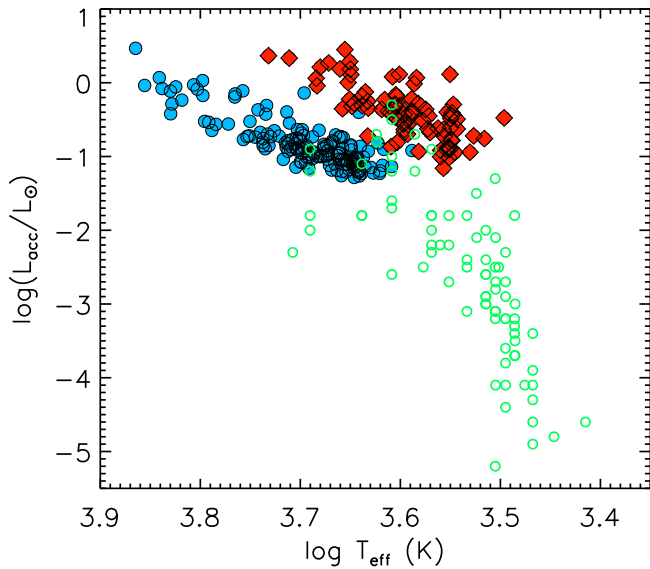


Figure 9. Accretion luminosity versus effective temperature. Filled circles and diamonds are as in Fig. 5. The Galactic Lupus objects by Alcalá et al. (2017) are overlaid as open circles.

pears to be similar for both lower-mass (i.e. $\simeq -0.72$) and higher-mass (i.e. $\simeq -0.70$) regimes and in good agreement with those measured in other MCs environments (see De Marchi et al. 2011, 2013, 2017). The shaded region in the same figure represents the prediction of viscous disk evolution by Hartmann et al. (1998). These models are able to reproduce the observed decreasing trend of \dot{M}_{acc} with age for low-mass T-Tauri stars in star-forming regions in the solar neighbourhood (see dotted region in the same figure and Hartmann et al. 2016 for a recent review on this issue⁵). The slope of this trend appears to be steeper than those obtained by us both for lower and higher-mass regimes ($\simeq -1.4$ against $\simeq -0.7$). This means that in the PMS candidates of LH 95 \dot{M}_{acc} decreases more slowly with time than what is observed for low-mass T-Tauri stars in Galactic star-forming regions close to the Sun ($\lesssim 1$ kpc; Sicilia-Aguilar et al. 2010). This behaviour supports the recent suggestions by De Marchi et al. (2017) according to which when metallicity is higher, like in the local neighbourhood, there are more dust grains in the disk and therefore the radiation pressure is higher, limiting the accretion process in both its rate and duration, while the mass accretion process seems to last longer at low metallicity. Other authors (e.g., Yasui et al. 2009, 2010, 2016) have concluded that in some low-metallicity environments of the outer Galaxy the disk lifetimes are shorter than in star forming regions in the solar vicinity. However, these works use the dust content of circumstellar disks as a proxy for the total mass of the disks and their lifetimes, while here we measure directly the infall of the probably more abundant gas onto the stars. Therefore, the results of the two studies are not directly comparable. And indeed, our findings are in agreement with optical spectroscopic observations of SFRs in the Galactic anticenter (Cusano et al. 2011; Kalari & Vink 2015), which indicate that a significant fraction of the young stellar objects have preserved their accretion disks, despite the low metallicity. These authors conclude that disk survival may depend not only on metallicity, but also on other environmental physical conditions or properties of the central objects. Galli et al. (2015) have found the following empirical relationship between disk lifetime and stellar mass: $t_{\text{disk}} = 4 \times 10^6 (M_{\star}/M_{\odot})^{0.75}$. Such a kind of relationship was found by the authors for stars in the Taurus-Auriga association, i.e. with $Z \sim Z_{\odot}$, but similar results were previously obtained in other solar-metallicity environ-

⁵ We note that the same authors have pointed out that this linear fit could be the consequence of correlated errors between age and accretion rate.

ments (see the case of Lupus in Bertout et al. 2007). If applied to our PMS candidates, neglecting the effects due to different metallicity or binarity (to mention a few), this relationship would imply that disks around stars of $\sim 0.55 M_{\odot}$ (median mass of our younger PMS stars) survive for $t_{\text{disk}} \sim 2$ Myr, similar to the mean age of our younger population (~ 1 Myr). Disk dispersal time of the order of 2 Myr is quite at odds with the ages of the older PMS candidates, whose disks have not totally been dissipated even at several tens Myr. We are therefore led to believe that, unless the older episodes of star formation were much more intense than the most recent one, it is very likely that circumstellar disks live longer in these metal-poor environments.

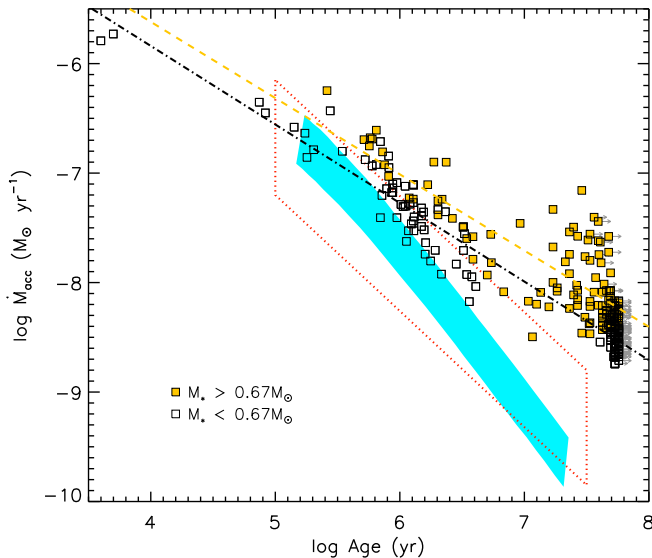


Figure 10. Mass accretion rate as a function of stellar age for our PMS candidates. The mean stellar mass is $\simeq 0.67 M_{\odot}$. Filled and open squares represent stars with M_{\star} larger than or smaller than the mean. Regression fits for these two sub-sample are represented with dashed and dot-dashed lines, respectively. Arrows indicate lower limits in stellar ages. The shaded region represents a collection of viscous disk evolutionary models taken from Hartmann et al. (1998) for solar-type stars with initial disk masses of $\sim 0.1 - 0.2 M_{\odot}$, constant viscosity $\alpha = 10^{-2}$, and viscosity exponent $\gamma = 1$ (for details see Sicilia-Aguilar et al. 2010). The dotted region shows the best linear fit and $\pm 1\sigma$ scatter obtained considering $0.3 - 1.0 M_{\odot}$ stars in Galactic SFRs (see the recent review by Hartmann et al. 2016).

5.4. Mass accretion rate versus Mass

Figure 11 shows \dot{M}_{acc} versus M_{\star} for all PMS candidates and contains several pieces of information in one

graph. Younger PMS candidates are marked with diamonds (red for ages younger than 1 Myr and green for 1 – 8 Myr), while older PMS candidates are represented by filled dots (the targets with ages of 8–16 Myr are highlighted in blue, while those older than 16 Myr are in black).

From a first glance, the stars in this plot appear to define a “fan-shaped” area. At a given stellar mass, we notice a wide spread in \dot{M}_{acc} for stars younger than 16 Myr. In particular, this spread in $\log \dot{M}_{\text{acc}}$ ranges from ~ 1 dex at $\sim 0.25 M_{\odot}$ up to ~ 2 dex at $\sim 0.67 M_{\odot}$, the mean mass of our targets. Splitting the sample of PMS stars in age bins, it is evident how the mass accretion rate is higher for younger stars, with mean values ranging from $\sim 2.6 \times 10^{-7} M_{\odot} \text{ yr}^{-1}$ for stars younger than 1 Myr (red diamonds), to $\sim 3.9 \times 10^{-8} M_{\odot} \text{ yr}^{-1}$ at $\sim 1 - 8$ Myr (green diamonds), to $\sim 1.1 \times 10^{-8} M_{\odot} \text{ yr}^{-1}$ for the stars with ages of $\sim 8 - 16$ Myr (blue circles). It is also clear that the slope of the $\dot{M}_{\text{acc}} - M_{\star}$ relationship changes according to the stellar age, ranging from ~ 0.0 for ages younger than 1 Myr, to ~ 1.0 between 1 and 8 Myr, up to ~ 4 for 8 – 16 Myr and older stars. Therefore, we conclude that attempting to define a relationship between \dot{M}_{acc} and M_{\star} without taking the age of the star into account can give spurious results and should be avoided⁶.

Another result we would like to point out concerns the slope of our targets younger than 16 Myr. In Fig. 11, we show with dashed lines the trends obtained, at given ages (0.25, 0.50, 1, 2, 4, 8, 16 Myr), considering the relationship between $\log \dot{M}_{\text{acc}}$ and $(\log M_{\star}, \log t)$ by De Marchi et al. (2017) and fixing as coefficients related to age and mass those obtained for the mass range $0.5 - 1.5 M_{\odot}$, i.e. $a = -0.59$ and $b = 0.78$ (see their Eq. 3), and as constant c , mainly related to the metallicity, that obtained by the same authors for 30 Doradus in the LMC (i.e. $c = -3.67$; see their Table 1), which we assume to be at the same metallicity as LH 95. Considering our LH 95 targets with ages younger than 1 Myr and in the same mass range, the slope of the $\log \dot{M}_{\text{acc}} - \log M_{\star}$ (~ 1 , solid line) is similar to that obtained by De Marchi et al. (2017) for 1 Myr stars in 30 Doradus. The slope of these targets is also similar to that found by Alcalá et al. (2017) for $0.5 - 1.5 M_{\odot}$ stars in the Galactic Lupus SFR at $\sim 1 - 3$ Myr (dot-dashed line). This latter qualitative comparison seems to suggest that Galactic and extragalactic SFRs share similar slope of the $\log \dot{M}_{\text{acc}} - \log M_{\star}$ relation. Moreover, this result also

⁶ We highlight here that part of the non detection of weakly accreting PMS candidates with high mass is due to our stringent selection (see Sect. 3.2).

implies that the age is a parameter acting on the objects we can detect, as more massive targets reach the main sequence faster than lower mass objects and consequently have lower levels of H α emission, thus causing the fan-shape of Fig. 11. This supports again the inter-correlation between mass accretion rate, mass, and age at given surrounding environments.

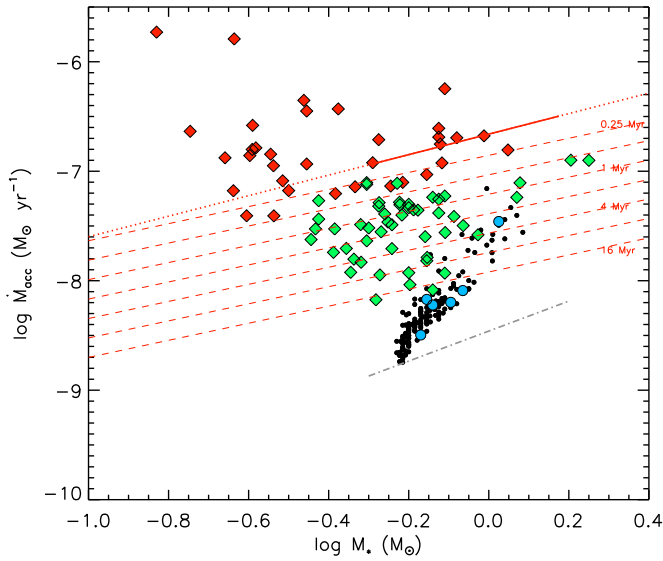


Figure 11. Mass accretion rate versus stellar mass for the younger PMS candidates (filled diamonds) and older PMS candidates (filled circles). Colors refer to the PMS candidates with different ages (red: ≤ 1 Myr, green: 1 – 8 Myr, blue: 8 – 16 Myr, black: > 16 Myr). Solid line represents the fit to the targets younger than 1 Myr and with masses of $\sim 0.5 - 1.5 M_{\odot}$ (see text), while dotted line is the extension of this fit to lower and higher masses. Dashed lines represent the $\log \dot{M}_{\text{acc}} - \log M_{\star}$ relationship obtained by De Marchi et al. (2017) at given ages (0.25, 0.50, 1, 2, 4, 8, 16 Myr) and considering in their Eq. 3 the a and b coefficients obtained for the same mass range ($0.5 - 1.5 M_{\odot}$) and ages (< 16 Myr) and c coefficient obtained for 30 Doradus, which we assume to be at the same metallicity as LH 95. Dash-dotted line is the $\log \dot{M}_{\text{acc}} - \log M_{\star}$ relationship obtained by Alcalá et al. (2017) for stars with $M_{\star} \sim 0.5 - 1.5 M_{\odot}$ in the Galactic Lupus star-forming region.

5.5. Mass accretion rate versus stellar Age and Mass in the context of the Large Magellanic Cloud

Assuming that all stars in our sample formed under similar conditions, we can study the simultaneous dependence of \dot{M}_{acc} on both M_{\star} and t through a multivariate least-squares fit of the type $\dot{M}_{\text{acc}} \propto t^a \times M_{\star}^b$. Adopting this simple relationship in the mass range

$0.5 - 1.5 M_{\odot}$ and for stars younger than 16 Myr, De Marchi et al. (2017) found $a \sim -0.6$ and $b \sim 1.3$ for ~ 300 stars in 30 Doradus in the LMC. If we consider the 54 objects with these characteristics in our LH 95 sample, we find $a \sim -1.1$ and $b \sim 1.3$. We indeed are cautious about this result because of a relatively few number of targets. Therefore, we now compare the mass accretion properties of the stars in LH 95 with those in several SFRs of our Galaxy and the Magellanic Clouds obtained with the same method. This provides us quantitative information on the effects of the environment during the final stages of the star formation. Following the prescriptions given by De Marchi et al. (2017), it is convenient to use a power-law dependence on mass and age like

$$\log \dot{M}_{\text{acc}} = a \times \log \frac{t}{\text{Myr}} + b \times \log \frac{M_{\star}}{M_{\odot}} + c, \quad (6)$$

where the c term reflects environmental effects, such as the metallicity, on the mass accretion rate. These authors studied a homogeneous sample of 1307 objects with $0.5 - 1.5 M_{\odot}$ younger than 16 Myr in six regions of the Milky Way, LMC, and SMC and analyzed them with the same method as our targets, finding $a = -0.59 \pm 0.02$ and $b = 0.78 \pm 0.08$, respectively. Using the same values of a and b also for the PMS candidates in LH 95 with the same restriction in mass and age, we derive $c = -3.54$. This latter value is consistent with the results for the two clusters in the LMC analyzed by the authors (namely, 30 Doradus and the SN1987A field) and more generally with their relationship $c = (-3.69 \pm 0.02) - (0.30 \pm 0.04) \log Z/Z_{\odot}$ obtained for the six clusters in the LMC, SMC, and the MW (see their Table 1). In particular, our value is between -3.41 obtained in NGC 346 (a cluster in the SMC with $Z \sim 0.002$) and -3.65 found for the MW clusters Trumpler 14 and NGC 3603 with $Z \sim Z_{\odot}$. Even if we do not draw more quantitative conclusions here, our analysis confirms the importance of considering cluster metallicity, besides stellar mass and age, when mass accretion is studied in different environments. Clearly, other physical conditions (like mean gas density or local magnetic field) of the environment might have an effect on the extend and duration of the star formation process in general, and on the evolution of the mass accretion rate, as suggested by De Marchi et al. (2017).

6. SUMMARY AND CONCLUSIONS

We have applied to the young association LH 95 in the Large Magellanic Cloud a photometric detection method to reliably identify PMS candidates actively undergoing mass accretion in a resolved stellar population without

requiring spectroscopic observations. The method combines HST wide-band $F555W$ and $F814W$ photometry with narrow-band $F658N$ imaging to *i*) identify stars with $H\alpha$ excess using as a reference template of the photospheric level the mean $m_{555} - m_{658}$ color of normal stars with very small photometric uncertainties; *ii*) convert the excess $H\alpha$ magnitude into luminosity and equivalent width; *iii*) derive accretion luminosity and mass accretion rate with similar accuracy as allowed by spectral line analysis. The main results of our study are summarized in the following items.

1. From the original photometric catalogue of 24515 sources, we extracted 1294 targets, taken as reference for our selection of PMS candidates, as they have errors in all three bands of less than 0.05 mag. Then, we identified 245 low-mass PMS candidates as those having $m_{555} - m_{658}$ color exceeding that of the reference stars by at least four times the photometric uncertainty at the same $m_{555} - m_{814}$ color.
2. From the measured $H\alpha$ luminosity of these PMS candidates, we derived the accretion luminosity and, through other stellar physical parameters obtained thanks to the [Bessell et al. \(1998\)](#) stellar atmospheric models, [Pecaut & Mamajek \(2013\)](#) calibrations, and evolutionary tracks by [Bressan et al. \(2012\)](#), their mass accretion rates. The PMS candidates have a median value of the mass accretion rate of $\sim 7.5 \times 10^{-9} M_{\odot} \text{ yr}^{-1}$.
3. Within the sample of PMS candidates we have identified two populations, which we call younger PMS candidates ($t \lesssim 8 \text{ Myr}$; median age of $\sim 1 \text{ Myr}$) and older PMS candidates ($9 \lesssim t \lesssim 60 \text{ Myr}$; median age of $\sim 50 \text{ Myr}$) with higher median values of the mass accretion rate for the former group compared to the latter ($\sim 5.4 \times 10^{-8} M_{\odot} \text{ yr}^{-1}$ against $\sim 4.8 \times 10^{-9} M_{\odot} \text{ yr}^{-1}$).
4. We have studied how the mass accretion rate changes with time as our PMS candidates approach the main sequence. We find that \dot{M}_{acc} decreases more slowly with time than what is predicted by models of viscous disk evolution ([Hartmann et al. 1998](#)) and observed for low-mass T-Tauri stars in Galactic star-forming regions within 1 kpc (e.g., [Sicilia-Aguilar et al. 2010](#); [Hartmann et al. 2016](#)). This is in line with previous findings in the Magellanic Clouds. Analyzing the $\dot{M}_{\text{acc}}-M_{\star}$ relationship, a clear dependence on age is evident, with a slope increasing with age.
5. We have studied the relationships between mass accretion rate, stellar mass and age, and we confirm previous findings obtained in the Magellanic Clouds, namely that attempts to derive correlations by fitting separately the observed dependence of \dot{M}_{acc} on M_{\star} or t may fail and introduce biases. Since these three stellar properties are intercorrelated, a proper multivariate fit is needed. Adopting for the PMS candidates in LH 95 a simple regression fit of the type $\dot{M}_{\text{acc}} \propto \text{Age}^a \times M_{\star}^b$ we find $a \sim -1.1$ and $b \sim 1.3$ for the mass range $0.5 - 1.5 M_{\odot}$ and ages younger than 16 Myr. Since the small number of targets, we are cautious about this result, and therefore we have also compared the mass accretion properties of the PMS in LH 95 with those homogeneously derived in several regions of the MW, LMC, and SMC (see next item).
6. We have applied to LH 95 the multivariate regression fit $\log \dot{M}_{\text{acc}} = a \times \log \frac{t}{\text{Myr}} + b \times \log \frac{M_{\star}}{M_{\odot}} + c$ of [De Marchi et al. \(2017\)](#) obtained for a uniform sample of 1307 PMS stars, with masses of $0.5 - 1.5 M_{\odot}$ and younger than 16 Myr contained in six different SFRs in the Milky Way, LMC, and SMC. The c value we find for LH 95 results to be close to that of the two regions in the LMC at the same metallicity (namely, 30 Doradus and the SN 1987A field). Moreover, it is lower than that achieved at lower- Z environments and higher than that found in solar-metallicity regions, thus confirming that metallicity is an important parameter to be taken into account when studying accretion properties and evolution.
7. We find that the younger PMS stars are clustered in sub-groups around early-type stars (mainly B type stars), while the older PMS stars are more uniformly distributed over the whole field of LH 95. We note that the presence of this sub-clustering suggests it may have its origin in short-lived parental molecular clouds within a giant molecular cloud complex, as in the case of Galactic OB associations (see, e.g., the Orion association; [Briceño et al. 2007](#)).
8. From a morphological study of age, spatial distribution, and accretion diagnostics, we find multiple generations of stars due to at least two star formation bursts, with the most recent one occurring some Myr ago and the previous one some tens Myr ago. The high values of \dot{M}_{acc} of the younger PMS stars and their vicinity to the early-type stars suggest that their circumstellar disks have not still considerably dispersed.

Since no infrared observations are available for this region, we can not draw any conclusion about the relationship between accretion properties and inner disk tracers. The advent of the *James Webb Space Telescope* will allow us to link mass accretion rate and grain properties. This will be also important to have information about the disk geometry and to explain which mechanisms allow circumstellar disks to feed their central PMS stars for tens of Myr in a low-metallicity, low-density environment such as the field of LH95 and give rise to a certain level of measurable mass accretion rate. Moreover, future spectroscopic observations of the region to derive accurate metallicity from the measurement, e.g., of the [O/H] ratio are very much needed if we want to understand the different contributions of metallicity and other effects, such as the environmental gas density, on the accretion process.

We thank our referee, Prof. Gregory Herczeg, whose extensive and insightful comments have helped us to improve the presentation of this work. KB is grateful to ESA for the support, via its Science Visitor programme, during the data analysis useful for the preparation of this

paper. KB also thanks the *Osservatorio Astronomico di Roma* for the hospitality during the preparation of the paper. This work was based on observations made with the NASA/ESA Hubble Space Telescope, and obtained from the Hubble Legacy Archive, which is a collaboration between the Space Telescope Science Institute (STScI/NASA), the Spacte Telescope European Coordinating Facility (ST-ECF/ESA) and the Canadian Astronomy Data Centre (CADC/NRC/CSA). Some of the data presented in this paper were obtained from the Mikulski Archive for Space Telescopes (MAST). STScI is operated by the Association of Universities for Research in Astronomy, Inc., under NASA contract NAS5-26555. This research made use of the SIMBAD database, operated at the CDS (Strasbourg, France) and data products from the Two Micron All Sky Survey, which is a joint project of the University of Massachusetts and the Infrared Processing and Analysis Center/California Institute of Technology, funded by the National Aeronautics and Space Administration and the National Science Foundation. This research has made also use of the SVO Filter Profile Service supported from the Spanish MINECO through grant AyA2014-55216.

APPENDIX

A. MASS, AGE, AND MASS ACCRETION RATE AS DETERMINED FROM DIFFERENT EVOLUTIONARY TRACKS AND ISOCHRONES

Masses and ages computed from different evolutionary tracks allow us to estimate the model-dependent uncertainty on the relationship between \dot{M}_{acc} and the stellar mass M_{\star} and age t .

In Fig. 12, we show the comparison between the masses, ages, and mass accretion rates as derived from two sets of PMS tracks for the same metallicity, namely the PARSEC stellar evolution model (Bressan et al. 2012) and the Pisa stellar models (Tognelli et al. 2011). Filled diamonds and circles refer to younger and older stars. The largest residuals between the two sets of tracks are seen for the younger low-mass stars, while for the older stars with higher masses the agreement is good (see panels *a* and *b*). In particular, the two sets of models differ significantly for $\log T_{\text{eff}}$ in the range $\sim 3.5 - 3.6$ and $\log L_{\star}$ in the range between $-0.8 L_{\odot}$ and $-0.1 L_{\odot}$, which translates into the spread in M_{\star} and \dot{M}_{acc} of young low-mass targets observed in panel *a* and *c* of Fig. 12. Squares in all three panels represent the 19 PMS younger stars departing from the 1:1 relation by twice the rms difference. The T_{eff} and L_{\star} values of these targets place them in an area of the HR diagram where the two sets of tracks are more discrepant most probably because of different treatment of the mixing length and opacity (P. Marigo, priv. comm.). In any case, the difference in mass of these 19 targets, representing 8% of the total sample with well determined masses and ages with both sets of tracks, affects the determination of the mass accretion rate slightly, with mean differences of about 0.2 dex in $\log M_{\star}$ between the PARSEC and Pisa models producing at most differences of about 0.2 dex in $\log \dot{M}_{\text{acc}}$. For the rest of the sample ($\sim 92\%$) the agreement in \dot{M}_{acc} is very good (panel *c*). Similar findings were also reported by Biazzo et al. (2014) in the case of L1616/L1615, a Galactic cometary cloud in the solar vicinity.

B. STELLAR PARAMETERS

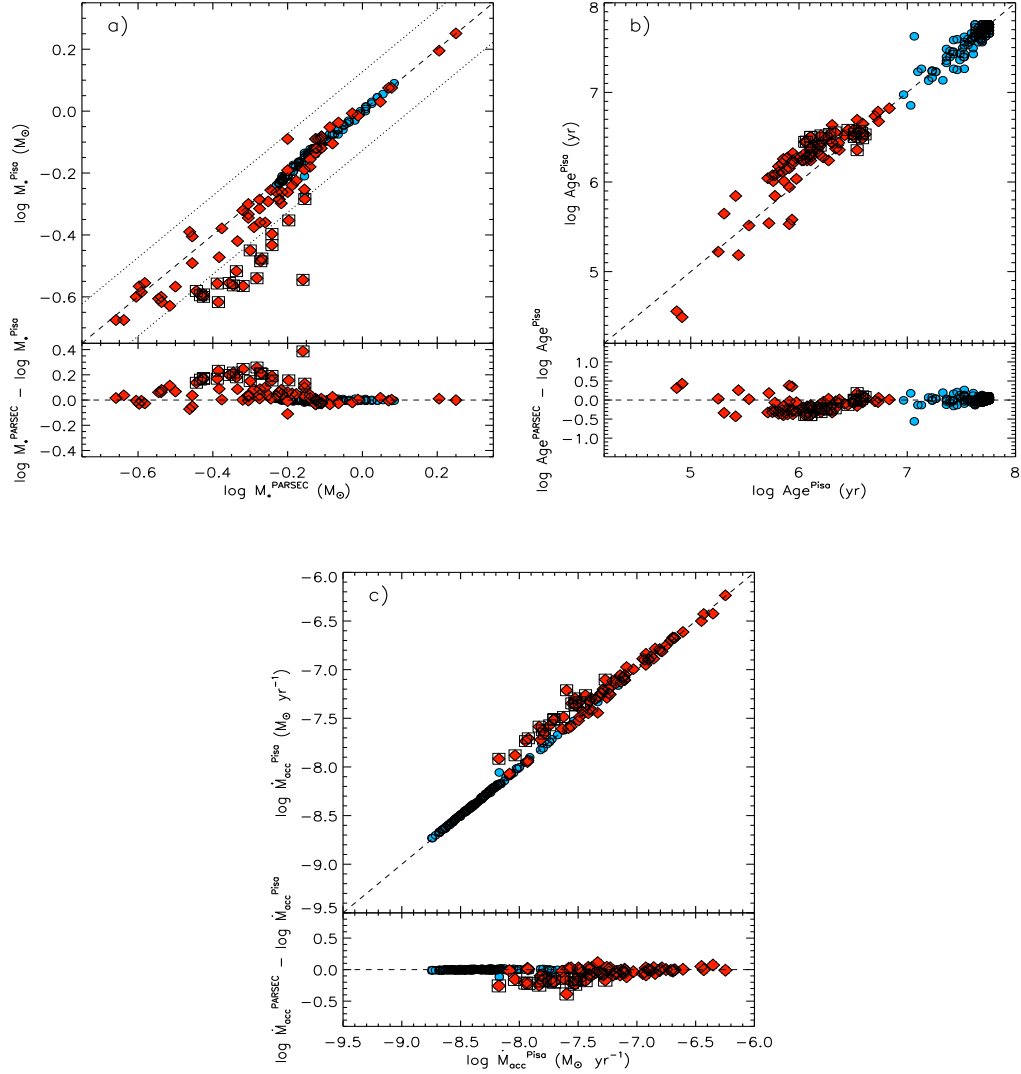


Figure 12. Comparison between masses (panel *a*), ages (panel *b*), and mass accretion rates (panel *c*) derived from the PARSEC and Pisa PMS models. Diamonds and circles refer to younger and older PMS stars. The dashed lines represent the 1:1 relation. The dotted lines in the panel *a*) are shifted by twice the rms difference between the $\log M_*$ values. Open squares mark the position of the targets outside the dotted lines in panel *a*).

Table 3. Stellar parameters of our sample of PMS accreting candidates. Columns list: object ID within our catalogue, right ascension, declination, dereddened magnitude in the *F555W*, *F814W*, and *F658N* bands, $H\alpha$ equivalent width, effective temperature, luminosity, mass, age, accretion luminosity, and mass accretion rate. Typical uncertainties in mass, age, $\log L_{\text{acc}}$, and $\log \dot{M}_{\text{acc}}$ are discussed in the text.

Number	RA	DEC	$(m_{555})_0$	$(m_{814})_0$	$(m_{658})_0$	$EW_{H\alpha}$	T_{eff}	L_*	M_*	$\log t$	$\log L_{\text{acc}}$	$\log \dot{M}_{\text{acc}}$
(ID)	(deg)	(deg)	(mag)	(mag)	(mag)	(Å)	(K)	(L_{\odot})	(M_{\odot})	(yr)	(L_{\odot})	(M_{\odot}/yr)
<i>Younger PMS candidates</i>												
100583	84.31741	-66.34244	21.873±0.010	21.014±0.010	20.977±0.089	14.9±1.5	5393±29	4.44±0.17	1.8	6.4	0.4	-6.9
100659	84.27160	-66.36848	21.991±0.013	20.738±0.011	20.773±0.061	18.7±1.0	4523±20	5.83±0.20	0.8	5.4	0.4	-6.2
101386	84.28833	-66.35663	23.130±0.016	22.046±0.011	21.999±0.064	19.9±1.0	4823±28	1.71±0.06	1.2	6.3	-0.0	-7.2

Table 3 continued

Table 3 (continued)

Number	RA	DEC	$(m_{555})_0$	$(m_{814})_0$	$(m_{658})_0$	$EW_{H\alpha}$	T_{eff}	L_*	M_*	$\log t$	$\log L_{\text{acc}}$	$\log \dot{M}_{\text{acc}}$
(ID)	(deg)	(deg)	(mag)	(mag)	(mag)	(Å)	(K)	(L_{\odot})	(M_{\odot})	(yr)	(L_{\odot})	(M_{\odot}/yr)
101473	84.29159	-66.36192	23.237±0.018	21.963±0.012	21.887±0.079	24.6±1.1	4490±20	1.88±0.06	0.8	5.9	0.0	-6.9
101511	84.27044	-66.36885	23.275±0.020	21.103±0.011	21.607±0.089	19.2±1.4	3551±10	4.65±0.13	0.2	3.6	0.1	-5.8
101783	84.29366	-66.35094	23.607±0.018	22.321±0.013	22.453±0.085	14.1±1.5	4474±20	1.35±0.04	0.8	6.1	-0.2	-7.2
101786	84.31878	-66.36094	23.610±0.022	22.205±0.011	22.206±0.103	23.1±1.5	4315±23	1.49±0.04	0.7	5.9	-0.1	-7.0
101906	84.26928	-66.36739	23.750±0.027	21.972±0.016	21.723±0.088	39.5±0.9	3836±28	2.11±0.05	0.4	4.9	0.1	-6.4
102386	84.30670	-66.36026	24.203±0.027	22.965±0.016	22.775±0.089	29.0±1.2	4548±37	0.75±0.02	0.9	6.6	-0.4	-7.6
102422	84.27140	-66.36541	24.236±0.030	22.855±0.016	22.668±0.178	31.0±2.2	4347±31	0.82±0.02	0.8	6.3	-0.3	-7.4
102483	84.30853	-66.35963	24.285±0.036	22.982±0.017	22.693±0.108	33.9±1.3	4451±37	0.73±0.01	0.9	6.5	-0.3	-7.5
102676	84.31286	-66.36160	24.464±0.034	22.936±0.020	22.798±0.118	31.2±1.5	4156±35	0.77±0.01	0.7	6.2	-0.4	-7.4
102769	84.29126	-66.36712	24.552±0.035	22.937±0.017	22.799±0.135	32.7±1.7	4046±35	0.78±0.01	0.6	6.1	-0.4	-7.3
102891	84.31294	-66.36579	24.640±0.032	22.892±0.015	22.856±0.175	31.2±2.2	3875±32	0.84±0.01	0.5	5.9	-0.4	-7.1
102986	84.27272	-66.36806	24.712±0.041	22.872±0.017	22.795±0.068	34.8±0.9	3756±34	0.99±0.01	0.4	5.8	-0.4	-6.9
103104	84.27522	-66.36653	24.800±0.040	23.114±0.019	23.295±0.096	20.0±1.6	3955±40	0.68±0.01	0.6	6.1	-0.6	-7.5
103237	84.28419	-66.35909	24.900±0.043	23.079±0.019	23.175±0.087	27.3±1.3	3781±40	0.82±0.01	0.4	5.9	-0.5	-7.2
103338	84.27172	-66.36070	24.969±0.051	23.345±0.032	22.669±0.260	49.3±1.9	4034±53	0.54±0.01	0.6	6.3	-0.3	-7.3
103348	84.31655	-66.36971	24.977±0.036	23.550±0.022	22.757±0.157	50.2±1.1	4286±40	0.43±0.01	0.8	6.7	-0.3	-7.6
103489	84.29056	-66.36341	25.079±0.045	23.417±0.022	22.682±0.164	51.1±1.2	3986±45	0.51±0.01	0.7	6.4	-0.3	-7.4
103560	84.27018	-66.36720	25.124±0.061	23.334±0.021	22.596±0.151	52.5±1.0	3821±58	0.62±0.01	0.5	6.0	-0.3	-7.1
103566	84.32519	-66.35709	25.128±0.046	23.383±0.020	22.440±0.204	56.0±1.1	3879±45	0.53±0.01	0.5	6.1	-0.2	-7.1
103652	84.33067	-66.37919	25.182±0.042	22.940±0.026	22.629±0.066	50.0±0.6	3524±13	0.85±0.01	0.3	5.2	-0.3	-6.6
103776	84.30940	-66.36179	25.283±0.052	23.271±0.034	22.891±0.092	47.5±0.8	3574±46	0.72±0.01	0.3	5.3	-0.4	-6.9
103819	84.27144	-66.36389	25.320±0.053	23.600±0.021	23.308±0.105	39.9±1.2	3911±51	0.44±0.01	0.5	6.2	-0.6	-7.5
103825	84.29388	-66.36495	25.327±0.052	23.611±0.028	23.633±0.193	28.1±2.7	3916±54	0.43±0.01	0.5	6.2	-0.7	-7.6
103914	84.26993	-66.36562	25.389±0.058	23.695±0.024	23.574±0.120	33.5±1.6	3945±57	0.40±0.01	0.7	6.6	-0.7	-7.8
104186	84.26853	-66.35411	25.570±0.066	23.973±0.031	24.063±0.114	22.5±2.0	4068±65	0.30±0.01	0.7	6.8	-0.9	-8.1
104237	84.28295	-66.36111	25.605±0.058	23.479±0.034	23.479±0.171	38.8±1.8	3605±56	0.52±0.01	0.3	5.9	-0.6	-7.2
104260	84.29657	-66.34939	25.623±0.062	23.441±0.019	23.101±0.142	49.5±1.1	3546±17	0.54±0.01	0.3	5.9	-0.5	-7.0
104457	84.30190	-66.37620	25.741±0.072	24.047±0.027	23.478±0.048	47.5±0.7	3945±70	0.29±0.01	0.7	6.7	-0.6	-7.8
104609	84.29965	-66.37489	25.848±0.070	22.860±0.016	23.084±0.119	52.7±0.9	3135±21	1.36±0.02	0.2	3.7	-0.5	-5.7
104680	84.29765	-66.35389	25.884±0.063	23.896±0.038	23.710±0.047	41.6±0.7	3599±55	0.41±0.01	0.4	6.1	-0.7	-7.5
104742	84.33483	-66.38161	25.918±0.068	23.604±0.021	23.460±0.097	47.3±0.9	3493±39	0.46±0.01	0.3	6.0	-0.6	-7.1
104743	84.27491	-66.35468	25.918±0.071	23.641±0.021	24.254±0.098	17.9±2.0	3510±29	0.44±0.01	0.3	6.0	-0.9	-7.4
104889	84.30924	-66.36060	25.999±0.076	23.950±0.028	23.848±0.291	40.3±2.9	3535±60	0.39±0.01	0.4	6.1	-0.8	-7.5
104905	84.28243	-66.37018	26.006±0.080	24.131±0.031	23.581±0.156	49.5±1.3	3718±63	0.31±0.01	0.6	6.5	-0.7	-7.7
104961	84.31383	-66.36284	26.044±0.079	23.861±0.025	23.408±0.147	52.1±1.1	3546±22	0.37±0.01	0.4	6.1	-0.6	-7.3
104962	84.31038	-66.36000	26.044±0.073	23.852±0.025	23.843±0.057	40.7±0.9	3542±20	0.37±0.01	0.4	6.1	-0.8	-7.4
105165	84.29009	-66.35439	26.159±0.092	24.131±0.032	24.158±0.098	35.4±1.5	3557±72	0.32±0.01	0.4	6.2	-0.9	-7.7
105410	84.29890	-66.35005	26.283±0.090	23.788±0.022	23.695±0.136	49.8±1.2	3363±40	0.42±0.02	0.2	5.7	-0.7	-6.9
105418	84.31978	-66.36187	26.285±0.095	24.197±0.029	23.432±0.047	56.6±0.5	3650±82	0.27±0.01	0.5	6.5	-0.6	-7.6
105464	84.31105	-66.35368	26.305±0.083	24.279±0.032	24.432±0.224	30.5±3.0	3559±66	0.28±0.01	0.5	6.3	-1.0	-7.9
105643	84.33208	-66.37099	26.400±0.099	24.294±0.030	24.401±0.199	34.5±2.5	3629±82	0.25±0.01	0.5	6.6	-1.0	-7.9
105709	84.28530	-66.35606	26.432±0.098	24.449±0.036	24.792±0.022	20.5±1.5	3605±77	0.24±0.01	0.5	6.6	-1.2	-8.2
105710	84.30597	-66.35695	26.433±0.090	24.409±0.034	24.071±0.265	46.6±2.2	3561±71	0.25±0.01	0.5	6.5	-0.9	-7.8
105729	84.28271	-66.35492	26.445±0.095	23.816±0.025	23.788±0.145	51.1±1.2	3281±37	0.42±0.02	0.2	5.2	-0.8	-6.6
200884	84.25101	-66.36951	22.206±0.014	21.259±0.010	21.059±0.178	24.8±2.5	5142±31	3.48±0.12	1.6	6.3	0.3	-6.9
201022	84.24808	-66.35949	22.400±0.014	21.299±0.011	21.365±0.090	14.1±1.6	4787±27	3.43±0.12	1.1	5.9	0.2	-6.8
201076	84.25639	-66.36952	22.478±0.012	21.327±0.011	21.225±0.107	23.7±1.6	4695±19	3.37±0.12	1.0	5.8	0.3	-6.7
201235	84.24942	-66.35973	22.694±0.014	21.472±0.013	21.424±0.138	22.3±2.1	4575±22	2.96±0.10	0.8	5.7	0.2	-6.7
201461	84.26330	-66.36691	22.928±0.015	21.848±0.013	21.741±0.093	22.7±1.4	4832±30	2.05±0.07	1.2	6.2	0.1	-7.1
201512	84.26661	-66.36714	22.976±0.025	21.681±0.017	21.620±0.162	24.2±2.4	4462±28	2.44±0.06	0.8	5.8	0.1	-6.8
201570	84.24540	-66.36099	23.038±0.017	21.747±0.012	21.436±0.223	34.6±2.6	4467±19	2.29±0.07	0.8	5.8	0.2	-6.7
201673	84.23938	-66.34700	23.146±0.017	21.859±0.014	21.176±0.076	46.3±0.6	4473±20	2.07±0.06	0.8	5.8	0.3	-6.6
202098	84.24630	-66.36020	23.544±0.025	21.885±0.014	21.610±0.155	38.4±1.6	3990±25	2.07±0.05	0.4	5.4	0.1	-6.4

Table 3 continued

Table 3 (continued)

Number	RA	DEC	$(m_{555})_0$	$(m_{814})_0$	$(m_{658})_0$	$EW_{H\alpha}$	T_{eff}	L_*	M_*	$\log t$	$\log L_{\text{acc}}$	$\log \dot{M}_{\text{acc}}$
(ID)	(deg)	(deg)	(mag)	(mag)	(mag)	(Å)	(K)	(L_{\odot})	(M_{\odot})	(yr)	(L_{\odot})	(M_{\odot}/yr)
202261	84.22890	-66.38596	23.699±0.018	21.937±0.012	21.931±0.061	30.3±0.8	3857±19	2.08±0.06	0.4	4.9	-0.0	-6.5
202575	84.24827	-66.35983	23.974±0.025	22.551±0.020	22.526±0.114	24.7±1.7	4291±29	1.08±0.03	0.7	6.1	-0.3	-7.2
202742	84.26123	-66.36847	24.107±0.031	22.556±0.015	22.465±0.057	29.7±0.8	4127±30	1.10±0.02	0.6	5.9	-0.2	-7.1
202761	84.25253	-66.36693	24.122±0.026	22.489±0.016	22.301±0.073	34.9±0.9	4023±27	1.18±0.03	0.5	5.8	-0.2	-6.9
202795	84.26528	-66.36755	24.152±0.040	22.543±0.018	21.693±0.055	53.0±0.4	4053±39	1.12±0.01	0.5	5.8	0.1	-6.7
202903	84.19248	-66.34855	24.232±0.026	22.852±0.015	22.354±0.089	42.0±0.9	4348±28	0.82±0.02	0.8	6.3	-0.2	-7.3
202916	84.24573	-66.36068	24.240±0.033	22.917±0.019	22.586±0.297	35.7±3.3	4425±35	0.78±0.01	0.8	6.4	-0.3	-7.4
203010	84.24858	-66.35919	24.319±0.030	22.692±0.016	22.616±0.176	30.5±2.2	4030±30	0.98±0.02	0.6	5.9	-0.3	-7.1
203019	84.24731	-66.35934	24.323±0.034	22.745±0.017	22.856±0.131	21.1±2.1	4092±34	0.93±0.01	0.6	6.0	-0.4	-7.3
203097	84.24862	-66.36884	24.388±0.028	22.793±0.015	22.911±0.099	21.0±1.6	4071±28	0.89±0.02	0.6	6.0	-0.4	-7.3
203406	84.24845	-66.36102	24.623±0.035	22.992±0.020	23.062±0.130	24.1±1.9	4025±36	0.74±0.01	0.6	6.1	-0.5	-7.4
203473	84.23920	-66.36548	24.672±0.036	23.033±0.018	22.351±0.218	49.6±1.6	4015±36	0.72±0.01	0.6	6.1	-0.2	-7.1
203480	84.24783	-66.35997	24.678±0.041	22.988±0.027	22.973±0.162	29.1±2.2	3950±44	0.76±0.01	0.5	6.0	-0.4	-7.3
203840	84.24845	-66.36369	24.935±0.042	23.512±0.023	23.704±0.075	13.5±1.5	4291±44	0.45±0.01	0.8	6.7	-0.7	-7.9
204035	84.24983	-66.36026	25.077±0.052	23.347±0.028	23.051±0.260	40.2±2.6	3898±53	0.55±0.01	0.6	6.2	-0.5	-7.4
204063	84.26327	-66.36600	25.100±0.050	23.405±0.024	23.259±0.198	34.4±2.3	3943±50	0.52±0.01	0.7	6.5	-0.5	-7.6
204149	84.23152	-66.36654	25.158±0.040	23.408±0.020	22.894±0.058	46.8±0.6	3872±40	0.52±0.01	0.5	6.2	-0.4	-7.3
204358	84.24573	-66.35980	25.287±0.058	23.082±0.021	23.009±0.244	43.0±2.3	3537±16	0.75±0.01	0.3	5.3	-0.4	-6.8
204645	84.25251	-66.36754	25.486±0.048	23.843±0.026	23.918±0.074	24.2±1.3	4010±49	0.34±0.01	0.6	6.5	-0.8	-7.9
204708	84.25025	-66.36051	25.530±0.075	23.217±0.024	23.126±0.199	45.9±1.7	3494±43	0.65±0.01	0.3	5.5	-0.5	-6.8
204775	84.20983	-66.36929	25.572±0.054	23.715±0.023	23.454±0.212	41.3±2.1	3737±43	0.45±0.01	0.5	6.2	-0.6	-7.5
204836	84.24826	-66.36148	25.609±0.072	23.395±0.024	22.914±0.134	53.1±0.9	3534±20	0.56±0.01	0.3	5.9	-0.4	-6.8
204896	84.19803	-66.36023	25.654±0.053	23.640±0.021	24.103±0.077	15.3±1.6	3572±42	0.51±0.01	0.3	5.8	-0.9	-7.4
205280	84.26629	-66.37236	25.917±0.073	24.124±0.034	24.228±0.162	26.3±2.4	3817±72	0.30±0.01	0.6	6.6	-0.9	-8.0
205303	84.24829	-66.36506	25.934±0.074	23.900±0.030	24.124±0.011	27.7±1.0	3551±59	0.40±0.01	0.4	6.1	-0.9	-7.6
205453	84.25227	-66.35344	26.021±0.082	24.156±0.030	23.020±0.141	60.0±0.7	3729±65	0.30±0.01	0.6	6.5	-0.5	-7.5
205455	84.25505	-66.36796	26.022±0.074	24.061±0.027	24.184±0.166	29.9±2.3	3628±58	0.35±0.01	0.5	6.2	-0.9	-7.8
205790	84.24213	-66.35971	26.220±0.082	24.069±0.030	24.180±0.238	35.6±2.8	3576±41	0.30±0.01	0.4	6.3	-0.9	-7.7
205990	84.23206	-66.34531	26.322±0.088	23.874±0.027	24.248±0.278	34.8±3.3	3392±40	0.39±0.01	0.2	5.9	-0.9	-7.2
<i>Older PMS candidates</i>												
100952	84.32237	-66.36344	22.520±0.012	21.902±0.013	21.820±0.081	12.7±1.5	6277±56	2.15±0.08	1.1	7.2	0.0	-7.3
100959	84.26922	-66.36774	22.528±0.021	22.064±0.022	21.720±0.151	24.0±2.2	6934±92	2.05±0.06	1.2	>7.6	0.1	-7.4
100973	84.29169	-66.36190	22.545±0.012	22.135±0.014	21.985±0.064	13.2±1.1	7172±57	2.01±0.07	1.2	>7.5	-0.0	-7.6
101478	84.32236	-66.36340	23.241±0.017	22.622±0.016	22.325±0.161	23.9±2.3	6272±71	1.11±0.03	1.0	>7.6	-0.2	-7.6
101503	84.32544	-66.33817	23.267±0.025	22.716±0.021	22.483±0.115	19.8±1.8	6584±84	1.06±0.03	1.0	>7.6	-0.2	-7.7
101505	84.29621	-66.34878	23.273±0.017	22.763±0.015	22.611±0.053	14.8±0.9	6736±60	1.05±0.03	1.0	>7.6	-0.3	-7.8
101794	84.29124	-66.36714	23.622±0.021	22.771±0.016	22.663±0.051	18.6±0.9	5417±57	0.88±0.02	1.0	7.2	-0.3	-7.7
101828	84.31632	-66.36279	23.660±0.019	22.929±0.015	22.377±0.141	36.0±1.6	5828±65	0.79±0.02	0.9	7.5	-0.2	-7.6
101864	84.33022	-66.37055	23.698±0.018	22.881±0.017	22.811±0.086	15.9±1.5	5525±55	0.80±0.02	0.9	7.4	-0.4	-7.7
101947	84.27251	-66.36078	23.792±0.028	23.287±0.025	22.945±0.161	24.4±2.3	6755±100	0.65±0.01	0.9	>7.6	-0.4	-8.0
102266	84.32281	-66.37748	24.089±0.023	23.425±0.021	23.303±0.094	15.8±1.6	6086±88	0.52±0.01	0.9	7.6	-0.6	-8.1
102449	84.29354	-66.34358	24.260±0.025	23.312±0.018	23.258±0.075	17.6±1.3	5139±57	0.53±0.01	0.9	7.4	-0.5	-7.9
102510	84.27681	-66.35836	24.317±0.030	23.667±0.024	23.510±0.069	17.4±1.2	6143±110	0.42±0.01	0.8	7.6	-0.6	-8.2
102776	84.26749	-66.34370	24.559±0.032	23.575±0.021	23.481±0.062	20.4±1.1	5045±65	0.41±0.01	0.8	7.4	-0.6	-8.0
102784	84.31930	-66.34799	24.566±0.030	23.790±0.022	23.718±0.097	15.2±1.7	5666±90	0.35±0.01	0.8	>7.7	-0.7	-8.2
102912	84.32805	-66.34791	24.657±0.030	23.895±0.023	23.819±0.065	15.1±1.2	5714±91	0.32±0.01	0.8	>7.7	-0.8	-8.3
102964	84.29495	-66.36967	24.695±0.033	23.870±0.027	23.574±0.133	27.1±1.9	5497±91	0.32±0.01	0.8	7.7	-0.7	-8.2
103085	84.31777	-66.36240	24.784±0.037	23.882±0.025	23.702±0.085	23.1±1.4	5261±83	0.31±0.01	0.8	>7.8	-0.7	-8.2
103112	84.26605	-66.34971	24.805±0.041	23.957±0.030	22.957±0.246	50.2±1.7	5427±111	0.30±0.01	0.8	7.7	-0.4	-7.9
103234	84.26518	-66.34048	24.899±0.043	23.903±0.025	23.840±0.082	19.0±1.5	5013±78	0.30±0.01	0.8	7.7	-0.8	-8.2
103235	84.32830	-66.36450	24.899±0.039	24.063±0.029	23.910±0.083	20.6±1.4	5463±105	0.27±0.01	0.8	>7.8	-0.8	-8.3
103256	84.29654	-66.35818	24.917±0.041	24.110±0.028	23.738±0.188	30.1±2.4	5559±113	0.26±0.01	0.7	>7.8	-0.7	-8.3
103399	84.30085	-66.37431	25.015±0.043	23.772±0.027	23.753±0.078	21.3±1.4	4540±56	0.36±0.01	0.8	7.3	-0.7	-8.1

Table 3 continued

Table 3 (continued)

Number	RA	DEC	$(m_{555})_0$	$(m_{814})_0$	$(m_{658})_0$	$EW_{H\alpha}$	T_{eff}	L_*	M_*	$\log t$	$\log L_{\text{acc}}$	$\log M_{\text{acc}}$
(ID)	(deg)	(deg)	(mag)	(mag)	(mag)	(Å)	(K)	(L_{\odot})	(M_{\odot})	(yr)	(L_{\odot})	(M_{\odot}/yr)
103452	84.27387	-66.35526	25.055±0.042	24.094±0.030	23.816±0.178	28.5±2.4	5105±94	0.25±0.01	0.7	>7.8	-0.8	-8.2
103515	84.29445	-66.36017	25.094±0.046	23.910±0.029	23.902±0.083	19.7±1.5	4639±64	0.31±0.01	0.8	7.4	-0.8	-8.2
103517	84.29024	-66.33946	25.095±0.043	24.092±0.029	24.138±0.050	13.3±1.1	4996±78	0.25±0.01	0.7	>7.7	-0.9	-8.3
103545	84.30585	-66.37456	25.109±0.046	24.168±0.033	23.862±0.064	29.4±1.0	5157±104	0.24±0.01	0.7	>7.8	-0.8	-8.2
103583	84.32980	-66.35082	25.138±0.058	24.197±0.040	23.963±0.156	26.3±2.3	5157±131	0.23±0.01	0.7	7.7	-0.8	-8.3
103644	84.27910	-66.36184	25.177±0.046	24.187±0.032	23.796±0.137	33.5±1.7	5029±89	0.23±0.01	0.7	7.5	-0.8	-8.2
103715	84.31757	-66.33519	25.230±0.043	24.393±0.034	24.029±0.107	30.2±1.5	5460±117	0.20±0.01	0.7	7.7	-0.9	-8.4
103717	84.31974	-66.38231	25.230±0.045	23.934±0.026	24.042±0.069	15.6±1.4	4461±48	0.31±0.01	0.8	7.1	-0.9	-8.2
103730	84.29031	-66.37573	25.238±0.047	24.249±0.030	24.074±0.129	24.4±2.0	5032±88	0.22±0.01	0.7	7.6	-0.9	-8.3
103786	84.32967	-66.37369	25.294±0.040	24.361±0.036	24.076±0.079	28.4±1.2	5178±98	0.20±0.01	0.7	>7.7	-0.9	-8.4
103815	84.30586	-66.38051	25.318±0.051	24.288±0.029	24.031±0.070	28.7±1.1	4938±88	0.21±0.01	0.7	7.7	-0.9	-8.3
103898	84.32343	-66.37184	25.383±0.049	24.221±0.030	23.968±0.176	30.6±2.3	4677±69	0.23±0.01	0.8	7.4	-0.8	-8.2
103926	84.32151	-66.38447	25.398±0.056	24.329±0.034	24.287±0.080	19.3±1.5	4855±98	0.21±0.01	0.7	7.7	-1.0	-8.4
103990	84.30760	-66.37855	25.446±0.057	24.403±0.033	24.312±0.133	21.3±2.2	4911±98	0.19±0.01	0.7	7.7	-1.0	-8.4
103998	84.32394	-66.37225	25.454±0.054	24.448±0.038	24.292±0.158	23.8±2.4	4989±99	0.18±0.01	0.7	7.6	-1.0	-8.4
104055	84.29799	-66.35120	25.492±0.048	24.373±0.036	24.132±0.209	29.4±2.8	4749±71	0.20±0.01	0.7	7.7	-0.9	-8.3
104080	84.29913	-66.36902	25.507±0.055	24.477±0.042	24.414±0.056	19.7±1.2	4938±103	0.18±0.01	0.7	>7.8	-1.0	-8.5
104086	84.29786	-66.36609	25.511±0.055	24.382±0.031	24.367±0.066	19.0±1.4	4732±75	0.20±0.01	0.7	7.7	-1.0	-8.4
104094	84.28131	-66.38257	25.516±0.060	24.371±0.033	24.195±0.126	27.0±1.9	4705±82	0.20±0.01	0.7	7.7	-0.9	-8.3
104107	84.32576	-66.37196	25.526±0.062	24.485±0.033	24.418±0.092	20.1±1.7	4915±105	0.18±0.01	0.7	>7.8	-1.0	-8.5
104266	84.31422	-66.36722	25.628±0.061	24.261±0.029	24.048±0.007	31.8±0.8	4366±64	0.22±0.01	0.7	7.4	-0.9	-8.2
104298	84.29190	-66.34444	25.652±0.064	24.540±0.037	24.381±0.033	25.7±1.0	4764±91	0.17±0.01	0.7	>7.8	-1.0	-8.4
104316	84.26365	-66.35498	25.661±0.068	24.314±0.032	24.457±0.003	14.7±1.2	4393±71	0.21±0.01	0.7	7.5	-1.0	-8.4
104426	84.33368	-66.36310	25.727±0.056	24.586±0.038	24.368±0.049	28.8±1.0	4712±80	0.17±0.01	0.7	7.7	-1.0	-8.4
104566	84.30245	-66.35672	25.813±0.066	24.772±0.043	24.791±0.047	15.6±1.4	4915±118	0.14±0.01	0.6	>7.8	-1.2	-8.6
104619	84.28295	-66.35082	25.855±0.072	24.858±0.040	24.573±0.095	29.4±1.5	5011±125	0.13±0.01	0.6	7.7	-1.1	-8.6
104642	84.29637	-66.34912	25.866±0.073	24.537±0.037	24.433±0.054	26.7±1.2	4417±77	0.17±0.01	0.7	7.7	-1.0	-8.4
104643	84.27788	-66.38097	25.866±0.087	24.660±0.040	24.360±0.126	33.0±1.8	4602±111	0.16±0.01	0.6	>7.7	-1.0	-8.4
104738	84.32780	-66.36165	25.917±0.078	24.682±0.035	24.500±0.108	28.6±1.7	4553±92	0.15±0.01	0.6	>7.8	-1.0	-8.4
104757	84.30210	-66.36574	25.927±0.077	24.694±0.039	24.513±0.099	28.6±1.6	4557±93	0.15±0.01	0.6	>7.8	-1.0	-8.5
104762	84.29932	-66.34977	25.928±0.064	24.592±0.037	24.477±0.098	27.3±1.6	4407±70	0.17±0.01	0.7	7.7	-1.0	-8.4
104781	84.32844	-66.35696	25.942±0.063	24.398±0.029	24.152±0.070	35.7±1.0	4136±62	0.20±0.01	0.7	7.2	-0.9	-8.2
104797	84.30850	-66.36185	25.952±0.068	24.689±0.036	24.502±0.211	29.3±2.9	4506±74	0.15±0.01	0.6	>7.8	-1.0	-8.4
104931	84.28252	-66.36729	26.027±0.093	24.715±0.043	24.490±0.081	31.5±1.5	4439±96	0.15±0.01	0.6	>7.8	-1.0	-8.4
105002	84.30695	-66.38393	26.066±0.075	24.725±0.041	24.421±0.045	35.0±1.0	4401±80	0.15±0.01	0.6	>7.8	-1.0	-8.4
105009	84.28341	-66.37871	26.070±0.082	24.819±0.047	24.484±0.075	35.0±1.3	4526±94	0.14±0.01	0.6	7.7	-1.0	-8.5
105084	84.33037	-66.37966	26.114±0.072	24.580±0.040	24.690±0.081	20.2±1.7	4148±73	0.17±0.01	0.7	7.5	-1.1	-8.5
105088	84.29739	-66.34153	26.116±0.062	24.822±0.041	24.549±0.222	33.2±2.7	4463±70	0.14±0.01	0.6	7.7	-1.1	-8.5
105103	84.29914	-66.37354	26.121±0.083	24.907±0.043	24.297±0.221	43.5±2.1	4589±106	0.13±0.01	0.6	>7.7	-1.0	-8.4
105147	84.30678	-66.37535	26.153±0.083	25.006±0.047	24.493±0.074	39.8±1.1	4702±113	0.11±0.01	0.6	>7.8	-1.0	-8.5
105168	84.28984	-66.35272	26.159±0.086	24.813±0.041	24.711±0.059	26.9±1.4	4394±90	0.14±0.01	0.6	7.7	-1.1	-8.5
105223	84.31408	-66.35240	26.182±0.084	24.837±0.037	24.836±0.082	22.2±1.8	4395±86	0.13±0.01	0.6	7.7	-1.2	-8.6
105280	84.32034	-66.33499	26.214±0.074	24.697±0.038	24.882±0.073	15.9±1.7	4170±74	0.15±0.01	0.7	7.6	-1.2	-8.5
105299	84.30460	-66.36235	26.223±0.084	25.008±0.047	24.269±0.232	47.1±2.0	4587±109	0.11±0.01	0.6	>7.8	-1.0	-8.4
105485	84.30917	-66.35639	26.314±0.084	25.002±0.050	24.681±0.027	35.2±1.0	4439±92	0.11±0.01	0.6	>7.8	-1.1	-8.5
105499	84.30689	-66.34977	26.322±0.086	25.380±0.055	24.216±0.124	54.3±0.9	5155±183	0.08±0.01	0.6	>7.8	-0.9	-8.6
105518	84.31413	-66.36744	26.335±0.089	25.160±0.054	23.865±0.094	58.0±0.6	4655±124	0.10±0.01	0.6	7.7	-0.8	-8.3
105523	84.32288	-66.34132	26.338±0.091	25.017±0.042	25.103±0.009	17.3±1.5	4427±95	0.11±0.01	0.6	>7.8	-1.3	-8.7
105531	84.30980	-66.34316	26.341±0.095	25.137±0.042	24.867±0.177	31.8±2.5	4606±120	0.10±0.01	0.6	>7.7	-1.2	-8.7
105617	84.29692	-66.38106	26.390±0.092	24.988±0.051	24.736±0.157	33.8±2.1	4319±97	0.11±0.01	0.6	>7.8	-1.1	-8.5
105618	84.33716	-66.37704	26.390±0.094	25.030±0.043	24.871±0.186	29.5±2.7	4375±97	0.11±0.01	0.6	>7.8	-1.2	-8.6
105629	84.29288	-66.36293	26.394±0.096	24.703±0.042	23.127±0.109	64.1±0.4	3948±95	0.16±0.01	0.7	7.3	-0.5	-7.8
105914	84.28570	-66.35744	26.538±0.089	25.092±0.049	24.764±0.201	37.2±2.3	4260±91	0.10±0.01	0.6	>7.7	-1.1	-8.6

Table 3 continued

Table 3 (continued)

Number	RA	DEC	$(m_{555})_0$	$(m_{814})_0$	$(m_{658})_0$	$EW_{H\alpha}$	T_{eff}	L_*	M_*	$\log t$	$\log L_{\text{acc}}$	$\log \dot{M}_{\text{acc}}$
(ID)	(deg)	(deg)	(mag)	(mag)	(mag)	(Å)	(K)	(L_{\odot})	(M_{\odot})	(yr)	(L_{\odot})	(M_{\odot}/yr)
105940	84.30993	-66.34090	26.547±0.095	25.391±0.052	24.695±0.064	45.4±1.0	4687±129	0.08±0.01	0.6	>7.8	-1.1	-8.7
201295	84.22925	-66.35225	22.757±0.013	22.165±0.014	21.964±0.060	18.8±1.0	6408±67	1.71±0.06	1.1	>7.6	-0.0	-7.4
201370	84.25741	-66.35658	22.840±0.014	22.237±0.015	22.110±0.060	15.0±1.1	6353±74	1.59±0.05	1.1	7.4	-0.1	-7.5
201488	84.20598	-66.36387	22.955±0.014	22.451±0.014	22.178±0.097	21.1±1.5	6759±51	1.40±0.05	1.1	>7.6	-0.1	-7.6
201790	84.24566	-66.36048	23.256±0.018	22.730±0.014	22.033±0.211	38.7±2.2	6676±61	1.07±0.03	1.0	7.4	-0.1	-7.6
201932	84.24048	-66.36494	23.396±0.018	22.664±0.015	22.271±0.141	29.9±1.8	5824±63	1.00±0.03	1.0	7.4	-0.2	-7.5
201954	84.25608	-66.35287	23.420±0.020	23.044±0.016	20.726±0.180	66.5±0.4	7323±79	0.90±0.03	1.0	7.5	0.5	-7.2
202333	84.26053	-66.36747	23.759±0.023	22.743±0.015	22.240±0.244	37.9±2.6	4968±40	0.89±0.02	1.1	7.0	-0.1	-7.5
202599	84.25690	-66.36718	23.990±0.029	23.351±0.021	23.235±0.070	15.0±1.3	6187±100	0.56±0.01	0.9	>7.7	-0.5	-8.1
202644	84.24506	-66.36098	24.025±0.029	23.551±0.025	22.090±0.110	56.8±0.6	6890±117	0.52±0.01	0.9	>7.7	-0.1	-7.7
202652	84.25620	-66.37402	24.030±0.026	23.406±0.021	23.203±0.077	19.4±1.3	6247±96	0.54±0.01	0.9	>7.7	-0.5	-8.1
202708	84.23724	-66.34436	24.074±0.025	23.287±0.019	23.203±0.078	16.0±1.4	5628±76	0.55±0.01	0.8	7.6	-0.5	-8.0
202776	84.24561	-66.35986	24.135±0.029	23.375±0.030	22.167±0.108	54.0±0.7	5721±101	0.51±0.01	0.9	>7.7	-0.1	-7.6
202830	84.24810	-66.37537	24.183±0.029	23.475±0.022	23.293±0.083	19.7±1.4	5915±97	0.48±0.01	0.9	>7.7	-0.6	-8.1
203320	84.23020	-66.37553	24.555±0.034	23.460±0.025	23.504±0.067	15.3±1.3	4800±60	0.47±0.01	0.9	7.2	-0.6	-8.0
203367	84.24718	-66.35929	24.594±0.035	23.658±0.026	22.882±0.087	45.4±0.8	5170±80	0.38±0.01	0.8	7.5	-0.4	-7.8
203375	84.27716	-66.39177	24.599±0.048	23.815±0.039	23.692±0.083	18.1±1.5	5638±149	0.34±0.01	0.8	7.6	-0.7	-8.2
203439	84.23264	-66.36665	24.645±0.034	23.643±0.026	23.602±0.075	18.0±1.3	4998±65	0.39±0.01	0.8	7.4	-0.7	-8.1
203478	84.26115	-66.36638	24.677±0.039	23.795±0.024	23.520±0.141	27.1±2.0	5322±95	0.34±0.01	0.8	7.6	-0.7	-8.1
203499	84.26345	-66.39032	24.689±0.035	23.834±0.030	23.635±0.065	23.2±1.1	5405±99	0.33±0.01	0.8	7.7	-0.7	-8.2
203605	84.21983	-66.38663	24.776±0.033	23.939±0.026	23.786±0.127	20.6±2.0	5460±91	0.30±0.01	0.8	>7.8	-0.8	-8.3
203619	84.25516	-66.37281	24.783±0.038	23.916±0.030	23.722±0.065	23.1±1.1	5368±103	0.31±0.01	0.8	>7.7	-0.7	-8.2
203809	84.22269	-66.36948	24.918±0.033	24.057±0.029	24.021±0.091	14.9±1.6	5387±94	0.27±0.01	0.8	7.7	-0.9	-8.4
203860	84.25838	-66.37823	24.947±0.044	23.730±0.025	23.742±0.119	19.2±2.0	4584±60	0.37±0.01	0.9	7.1	-0.7	-8.1
203873	84.25300	-66.38037	24.959±0.045	23.764±0.027	23.661±0.117	24.5±1.8	4621±62	0.36±0.01	0.8	7.3	-0.7	-8.0
203903	84.19118	-66.34936	24.980±0.040	24.001±0.030	23.774±0.137	26.6±1.9	5058±86	0.28±0.01	0.7	7.7	-0.8	-8.2
203930	84.24300	-66.36428	25.003±0.041	24.073±0.031	23.928±0.091	21.9±1.5	5186±95	0.26±0.01	0.8	>7.8	-0.8	-8.3
203954	84.24202	-66.35572	25.018±0.040	24.006±0.032	23.685±0.163	31.1±2.1	4977±77	0.28±0.01	0.7	7.7	-0.7	-8.1
203958	84.26858	-66.38790	25.021±0.043	24.175±0.036	24.132±0.071	15.0±1.4	5433±120	0.24±0.01	0.7	>7.8	-0.9	-8.4
204044	84.21298	-66.34674	25.082±0.039	24.109±0.026	23.968±0.124	22.5±1.9	5074±84	0.25±0.01	0.7	>7.7	-0.8	-8.3
204046	84.26278	-66.38299	25.083±0.048	24.130±0.032	24.149±0.073	13.8±1.5	5126±107	0.25±0.01	0.7	7.7	-0.9	-8.3
204220	84.20907	-66.37826	25.201±0.046	24.195±0.034	23.487±0.092	44.2±0.9	4989±85	0.23±0.01	0.7	7.7	-0.6	-8.1
204224	84.24075	-66.37636	25.208±0.053	24.224±0.031	24.182±0.094	17.7±1.7	5045±100	0.22±0.01	0.7	7.6	-0.9	-8.4
204245	84.24843	-66.39069	25.220±0.044	24.264±0.034	24.062±0.111	25.1±1.7	5118±103	0.22±0.01	0.7	7.7	-0.9	-8.3
204248	84.22416	-66.38059	25.223±0.052	24.221±0.032	24.263±0.044	13.4±1.2	4998±92	0.23±0.01	0.7	7.6	-0.9	-8.4
204500	84.23834	-66.38866	25.382±0.062	24.160±0.031	24.269±0.040	14.2±1.3	4575±81	0.25±0.01	0.7	7.5	-1.0	-8.3
204524	84.27125	-66.37828	25.402±0.081	24.259±0.049	24.210±0.067	21.0±1.6	4709±112	0.23±0.01	0.7	7.6	-0.9	-8.3
204575	84.26226	-66.36685	25.437±0.060	24.208±0.036	23.720±0.272	40.0±2.8	4564±79	0.24±0.01	0.8	7.4	-0.7	-8.1
204668	84.24878	-66.35863	25.502±0.058	24.380±0.038	24.069±0.170	32.3±2.2	4744±82	0.20±0.01	0.7	7.7	-0.9	-8.3
204698	84.25701	-66.36720	25.523±0.072	24.462±0.039	23.726±0.204	45.5±1.8	4872±123	0.18±0.01	0.7	>7.8	-0.7	-8.2
204728	84.20835	-66.36141	25.544±0.051	24.566±0.043	24.117±0.162	35.5±1.9	5060±111	0.16±0.01	0.7	7.7	-0.9	-8.4
204734	84.25307	-66.38390	25.545±0.058	24.527±0.040	24.104±0.240	35.1±2.8	4964±106	0.17±0.01	0.7	7.7	-0.9	-8.4
204736	84.21478	-66.35324	25.545±0.056	24.478±0.035	24.238±0.071	28.6±1.2	4860±100	0.18±0.01	0.7	>7.8	-0.9	-8.4
204762	84.24497	-66.37016	25.562±0.066	24.441±0.033	23.977±0.102	37.9±1.3	4746±88	0.19±0.01	0.7	7.7	-0.8	-8.3
204788	84.19713	-66.36378	25.582±0.076	24.443±0.039	24.018±0.130	36.8±1.6	4715±101	0.19±0.01	0.7	7.7	-0.8	-8.3
204806	84.23247	-66.36692	25.593±0.058	24.491±0.037	24.400±0.114	22.4±1.9	4785±89	0.18±0.01	0.7	>7.8	-1.0	-8.4
204817	84.25305	-66.35604	25.598±0.052	24.538±0.037	24.468±0.055	20.6±1.2	4875±95	0.17±0.01	0.7	7.1	-1.0	-8.5
204835	84.21503	-66.37206	25.608±0.059	24.688±0.040	24.491±0.146	24.2±2.3	5212±131	0.15±0.01	0.6	>7.8	-1.0	-8.6
204965	84.23400	-66.36196	25.695±0.062	24.606±0.043	24.393±0.130	27.7±1.9	4813±103	0.16±0.01	0.7	7.7	-1.0	-8.5
205004	84.25818	-66.36052	25.730±0.068	24.374±0.033	22.897±0.185	61.5±0.8	4381±71	0.20±0.01	0.7	7.5	-0.4	-7.8
205037	84.20301	-66.35402	25.750±0.069	24.749±0.035	24.586±0.150	24.0±2.4	5000±117	0.14±0.01	0.6	>7.8	-1.1	-8.6
205062	84.23379	-66.35196	25.770±0.058	24.471±0.036	24.171±0.276	34.3±3.3	4457±64	0.19±0.01	0.7	7.6	-0.9	-8.3
205181	84.20958	-66.36611	25.850±0.069	24.459±0.032	24.412±0.082	25.1±1.5	4334±71	0.19±0.01	0.7	7.5	-1.0	-8.4

Table 3 continued

Table 3 (continued)

Number	RA	DEC	$(m_{555})_0$	$(m_{814})_0$	$(m_{658})_0$	$EW_{H\alpha}$	T_{eff}	L_*	M_*	$\log t$	$\log L_{\text{acc}}$	$\log \dot{M}_{\text{acc}}$
(ID)	(deg)	(deg)	(mag)	(mag)	(mag)	(Å)	(K)	(L_{\odot})	(M_{\odot})	(yr)	(L_{\odot})	(M_{\odot}/yr)
205191	84.20804	-66.37716	25.860±0.064	24.565±0.034	24.000±0.182	43.1±1.7	4462±68	0.17±0.01	0.7	7.7	-0.8	-8.2
205209	84.21629	-66.35535	25.869±0.068	24.660±0.049	24.362±0.161	33.0±2.1	4597±99	0.16±0.01	0.7	7.7	-1.0	-8.4
205324	84.22818	-66.37878	25.943±0.071	24.794±0.041	24.309±0.266	38.9±2.8	4699±98	0.14±0.01	0.6	>7.8	-1.0	-8.4
205416	84.24755	-66.36277	26.004±0.080	24.765±0.048	24.108±0.275	45.1±2.4	4547±98	0.14±0.01	0.6	>7.8	-0.9	-8.3
205422	84.25428	-66.37085	26.006±0.090	24.737±0.040	24.649±0.119	25.0±2.1	4497±92	0.15±0.01	0.6	>7.8	-1.1	-8.5
205542	84.23473	-66.39123	26.073±0.061	24.823±0.041	24.657±0.207	28.2±2.9	4528±75	0.14±0.01	0.6	7.7	-1.1	-8.5
205676	84.24683	-66.39611	26.156±0.071	24.656±0.039	23.940±0.240	49.1±1.8	4191±72	0.16±0.01	0.7	7.5	-0.8	-8.2
205677	84.21790	-66.35429	26.157±0.084	24.922±0.037	24.896±0.004	21.5±1.3	4553±98	0.12±0.01	0.6	>7.7	-1.2	-8.6
205691	84.22599	-66.37111	26.163±0.082	24.973±0.045	24.637±0.045	34.2±1.1	4629±111	0.12±0.01	0.6	>7.7	-1.1	-8.6
205771	84.23836	-66.36691	26.210±0.094	24.992±0.049	24.485±0.055	40.4±1.1	4582±116	0.12±0.01	0.6	>7.7	-1.0	-8.5
205778	84.21813	-66.36502	26.214±0.091	24.467±0.061	24.191±0.049	39.9±1.0	3876±100	0.20±0.01	0.7	7.0	-0.9	-8.2
205779	84.23670	-66.36692	26.214±0.097	24.947±0.045	24.540±0.168	37.7±2.0	4500±100	0.12±0.01	0.6	7.7	-1.1	-8.5
205812	84.26352	-66.39044	26.235±0.090	25.258±0.054	24.755±0.174	37.4±2.1	5063±169	0.09±0.01	0.6	>7.7	-1.1	-8.7
205814	84.24798	-66.37376	26.235±0.095	24.923±0.052	24.546±0.218	37.2±2.5	4439±102	0.12±0.01	0.6	>7.7	-1.1	-8.5
205821	84.25049	-66.37525	26.238±0.095	24.911±0.041	24.647±0.205	33.3±2.7	4419±97	0.12±0.01	0.6	>7.7	-1.1	-8.5
205858	84.23908	-66.35177	26.260±0.083	24.978±0.048	24.832±0.193	27.8±2.8	4479±90	0.12±0.01	0.6	>7.8	-1.2	-8.6
205908	84.22574	-66.38602	26.280±0.086	25.256±0.057	24.607±0.206	42.7±2.0	4951±155	0.09±0.01	0.6	>7.7	-1.1	-8.7
205930	84.20727	-66.35808	26.291±0.096	25.121±0.046	24.852±0.208	31.3±2.8	4663±127	0.10±0.01	0.6	>7.8	-1.2	-8.7
205933	84.19588	-66.35396	26.293±0.092	24.918±0.050	24.971±0.083	20.0±1.9	4355±99	0.12±0.01	0.6	>7.8	-1.2	-8.6
205942	84.24585	-66.38506	26.298±0.087	24.978±0.063	24.783±0.087	30.5±1.5	4429±101	0.12±0.01	0.6	>7.8	-1.2	-8.6
205950	84.23575	-66.34881	26.302±0.084	24.993±0.042	24.594±0.224	37.9±2.5	4443±89	0.12±0.01	0.6	>7.8	-1.1	-8.5
205955	84.21502	-66.37797	26.305±0.085	24.878±0.045	24.216±0.173	47.0±1.5	4286±87	0.13±0.01	0.6	>7.7	-0.9	-8.3
205959	84.20051	-66.35242	26.307±0.079	24.705±0.040	24.734±0.080	25.4±1.6	4062±79	0.15±0.01	0.7	7.5	-1.1	-8.5
205980	84.19942	-66.36190	26.318±0.082	24.958±0.045	25.054±0.043	17.5±1.5	4375±88	0.12±0.01	0.6	>7.7	-1.3	-8.7
206061	84.23042	-66.37977	26.363±0.094	25.006±0.045	24.925±0.053	26.1±1.5	4379±98	0.11±0.01	0.6	>7.8	-1.2	-8.6
206092	84.20873	-66.36808	26.378±0.097	24.865±0.040	24.967±0.064	20.2±1.8	4175±94	0.13±0.01	0.6	7.7	-1.2	-8.6
206140	84.25296	-66.38738	26.404±0.090	25.089±0.049	24.657±0.158	39.1±1.8	4435±97	0.11±0.01	0.6	>7.8	-1.1	-8.6
206142	84.21244	-66.37968	26.405±0.085	25.173±0.051	25.045±0.130	26.2±2.1	4559±105	0.10±0.01	0.6	7.7	-1.3	-8.7
206269	84.24240	-66.39419	26.470±0.077	25.210±0.054	24.916±0.214	33.5±2.7	4511±91	0.09±0.01	0.6	>7.7	-1.2	-8.7
206357	84.19530	-66.34836	26.515±0.084	25.168±0.043	24.915±0.085	33.1±1.4	4393±89	0.10±0.01	0.6	>7.7	-1.2	-8.7
206419	84.23594	-66.39544	26.545±0.098	25.081±0.046	24.953±0.129	29.8±2.1	4237±97	0.11±0.01	0.6	7.7	-1.2	-8.6

REFERENCES

- Alcalá, J. M., Natta, A., Manara, C., et al. 2014, *A&A*, 561, A2
- Alcalá, J. M., Manara, C., Natta, A., et al. 2017, *A&A*, 600, A20
- Antoniucci, S., García-López, R., Nisini, B., et al. 2011, *A&A*, 534, 32
- Barentsen, G., Vink, J. S., Drew, J. E., et al. 2011, *MNRAS*, 415, 103
- Barentsen, G., Vink, J. S., Drew, J. E., & Sale, S. E. 2013, *MNRAS*, 429, 1981
- Biazzo, K., Frasca, A., Henry, G. W., Catalano, S., & Marilli, E. 2007, *ApJ*, 656, 474
- Biazzo, K., Alcalá, J. M., Covino, E., et al. 2012, *A&A*, 547, A104
- Biazzo, K., Alcalá, J. M., Frasca, A., et al. 2014, *A&A*, 572, A84
- Beccari, G., Spezzi, L., De Marchi, G., et al. 2010, *ApJ*, 720, 1108
- Beccari, G., De Marchi, G., Panagia, N., & Pasquini, L. 2014, *MNRAS*, 437, 2621
- Beccari, G., De Marchi, G., Panagia, N., et al. 2015, *A&A*, 574, A44
- Bertout, C., Siess, L., & Cabrit, S. 2007, *A&A*, 473, L21
- Bessell, M., Castelli, F., & Plez, B. 1998, *A&A*, 333, 231
- Bressan, A., Marigo, P., Girardi, L., et al. 2012, *MNRAS*, 427, 127
- Briceño, C., Calvet, N., Hernández, J., et al. 2005, *ApJ*, 129, 907
- Briceño, C., Hartmann, L., Hernández, J., et al. 2007, *A&A*, 661, 1119
- Briceño, C., Calvet, N., Hernández, J., et al. 2018, *AJ*, 157, 85

- Camenzind, D. 1990, *RvMA*, 3, 234
- Caratti o Garatti, A., García-López, R., Antonucci, S., et al. 2012, *A&A*, 538, A64
- Colucci, J. E., Bernstein, R. A., Cameron, S. A., & McWilliam, A. 2012, *ApJ*, 746, 29
- Costigan, G., Schözl, A., Stelzer, B., et al. 2012, *MNRAS*, 427, 1344
- Costigan, G., Vink, J. S., Schözl, A., Ray, T., & Testi, L. 2014, *MNRAS*, 440, 3444
- Cusano, F., Ripepi, V., Alcalá, J. M., et al. 2011, *MNRAS*, 410, 227
- Cutri, R. M., Skrutskie, M. F., van Dyk, S., et al. 2003, Explanatory Supplement to the 2MASS All Sky Data Release
- Dahm, S. 2008, *AJ*, 136, 521
- Da Rio, N., Gouliermis, D., & Henning, T. 2009, *ApJ*, 696, 528
- Da Rio, N., Gouliermis, D., & Gennaro, M. 2010, *ApJ*, 723, 166
- Da Rio, N., Gouliermis, D. A., Rochau, B. et al. 2012, *MNRAS*, 422, 3356
- De Marchi, G., Panagia, N., & Romaniello, M. 2010, *ApJ*, 715, 1
- De Marchi, G., Panagia, N., Romaniello, M., et al. 2011, *ApJ*, 740, 11
- De Marchi, G., Beccari, G., & Panagia, N. 2013, *ApJ*, 775, 68
- De Marchi, G., Panagia, N., & Beccari, G. 2017, *ApJ*, 846, 110
- Dobbie, P. D., Cole, A. A., Subramaniam, A., & Keller, S. 2014, *MNRAS*, 442, 1663
- Fang, M., Kim, J. S., van Boekel, R., et al. 2013, *ApJS*, 207, 5
- Fitzpatrick, E. L., & Savage, B. D. 1984, *ApJ*, 279, 578
- Frasca, A., Biazzo, K., Taş, G., Evren, S., & Lanzafame, A. C. 2008, *A&A*, 479, 557
- Galli, P. A. B., Bertout, C., Teixeira, R., & Ducourant, C. 2015, *A&A*, 580, A26
- Gilmozzi, R., Kinney, E. K., Ewald, S. P., Panagia, N., & Romaniello, M. 1994, *ApJ*, 435, L43
- Gouliermis, D., Brandner, W., & Henning, T. 2006, *ApJ*, 636, L133
- Gouliermis, D. A., Henning, T., Brandner, W., et al. 2007, *ApJ*, 665, L27
- Gouliermis, D., Keller, S. C., de Boer, K. S., Kontizas, M., & Kontizas, E. 2002, *A&A*, 381, 862
- Gullbring, E., Hartmann, L., Briceño, C., & Calvet, N. 1998, *ApJ*, 492, 323
- Hartigan, P., Edwards, S., & Ghandour, L. 1995, *ApJ*, 452, 736
- Hartmann, L. 1998: in *Accretion Processes in Star Formation*, Cambridge Univ. Press
- Hartmann, L., Calvet, N., Gullbring, E., & D'Alessio, P. 1998, *ApJ*, 495, 385
- Hartmann, L., Herczeg, G., & Calvet, N. 2016, in *Annual Review of Astronomy and Astrophysics*, 54, 135
- Henize, K. G. 1956, *ApJS*, 2, 315
- Herczeg, G. J., & Hillenbrand, L. A. 2008, *ApJ*, 681, 594
- Hillenbrand, L. A., Hoffer, A. S., & Herczeg, G. J. 2013, *ApJ*, 146, 85
- Kalari, V. M., & Vink, J. S. 2015, *ApJ*, 800, 113
- Königl, A. 1991, *ApJS*, 370, L39
- Kontizas, M., Kontizas, E., Dapergolas, A., Argyropoulos, S., & Bellas-Velidis, Y. 1994, *A&AS*, 107, 7
- Lucke, P. B., & Hodge, P. W. 1970, *AJ*, 75, 171
- Lucke, P. B. 1974, *ApJS*, 28, 73
- Luhman, K. L. 2007, *ApJS*, 173, 104
- Manara, C. F., Beccari, G., Da Rio, N., et al. 2013, *A&A*, 558, A114
- Manara, C. F., Testi, L., Herczeg, G. J., et al. 2017, *A&A*, 604, A127
- Mulders, G. D., Pascucci, I., Manara, C. F., et al. 2017, *ApJ*, 847, 31
- Muzerolle, J., Hartmann, L., & Calvet, N. 1998, *AJ*, 116, 2965
- Osterbrock, D. 1989, *Astrophysics of Gaseous Nebulae and Active Galactic Nuclei* (Mill Valley, CA: Univ. Science Books)
- Panagia, N. 1999, in *IAU Symp. 190, New Views of the Magellanic Clouds*, eds. Y.-H. Chu, N. Suntzeff, J. Hesser, & D. Bohlender, p. 549
- Panagia, N., Romaniello, M., Scuderi, S., & Kirshner, R. P. 2000, *ApJ*, 539, 197
- Pecaut, M. J., & Mamajek, E. E. 2013, *ApJS*, 208, 9
- Rigliaco, E., Natta, A., Randich, S., Testi, L., & Biazzo, K. 2011, *A&A*, 525, 47
- Rodrigo, C., Solano, E., & Bayo, A. 2012, *IWOA Working Draft 15*
- Romaniello, M. 1998, PhD thesis, Scuola Normale Superiore di Pisa
- Romaniello, M., Scuderi, S., Panagia, N., Salerno, R. M., & Blanco, C. 2006, *A&A*, 446, 955
- Rosotti, G. P., Clarke, C. J., Manara, C. F., & Facchini, S. 2017, *MNRAS*, 468, 1631
- Ryon, J. E., et al. 2018, "ACS Instrument Handbook", Version 17.0 (Baltimore: STScI)
- Sicilia-Aguilar, A., Henning, T., & Hartmann, L. W. 2010, *ApJ*, 710, 597
- Sirianni, M., Jee, M. J., Benítez, N., et al. 2005, *PASP*, 117, 1049

- Soderblom, D. R., Hillenbrand, L. A., Jeffries, R. D., Mamajek, E. E., & Naylor, T. 2014, in *Protostars and Planets VI*, University of Arizona Press, eds. H. Beuther, R. Klessen, C. Dullemond, & Th. Henning, p. 219
- Spezzi, L., De Marchi, G., Panagia, N., Sicilia-Aguilar, S., & Ercolano, B. 2012, *MNRAS*, 421, 78
- Spitzer, L. Jr, & Greenstein, J. L. 1951, *ApJ*, 114, 407
- Stetson, P. B. 1987, *PASP*, 99, 191
- Stetson, P. B. 1994, *PASP*, 106, 250
- Tognelli, E., Prada Moroni, P. G., & Degl'Innocenti, S. 2011, *A&A*, 533, A109
- Vorobyov, E. I., & Basu, S. 2009, *ApJ*, 703, 922
- White, R. J., & Basri, G. 2003, *ApJ*, 582, 1109
- White, R. J., & Hillenbrand, L. A. 2004, *ApJ*, 616, 998
- Yasui, C., Kobayashi, N., Tokunaga, A. T., Saito, M., & Tokoku, C. 2009, *ApJ*, 705, 54
- Yasui, C., Kobayashi, N., Tokunaga, A. T., Saito, M., & Tokoku, C. 2010, *ApJ*, 723, L113
- Yasui, C., Kobayashi, N., Saito, M., & Izumi, N. 2016, *ApJ*, 151, 115
- Zeidler, P., Grebel, E. K., Nota, A., et al. 2016, *ApJ*, 152, 84